mathematics

MDPI

Article

Adaptation of an Eddy Current Model for Characterizing Subsurface Defects in CFRP Plates Using FEM Analysis Based on Energy Functional

Mario Versaci [1], Filippo Laganà [2], Francesco Carlo Morabito [1], Annunziata Palumbo [3] and Giovanni Angiulli [4,*]

[1] Department of Civil, Energetic, Environmental and Material Engineering, Mediterranea University, Via Zehender, I-89122 Reggio Calabria, Italy; mario.versaci@unirc.it (M.V.); morabito@unirc.it (F.C.M.)
[2] Health Science Department, "Magna Graecia" University of Catanzaro, I-88100 Catanzaro, Italy; filippo.lagana@unicz.it
[3] MIFT Department, University of Messina, Via F. D'Alcontres 31, I-98122 Messina, Italy; apalumbo@unime.it
[4] Department of Information Engineering, Infrastructures and Sustainable Energy, Mediterranea University, Via Zehender, I-89122 Reggio Calabria, Italy
* Correspondence: giovanni.angiulli@unirc.it

Abstract: In this work, a known Eddy Current (EC) model is adapted to characterize subsurface defects in carbon fiber-reinforced polymer (CFRP) plates intended for the civil aerospace industry. The considered defects include delaminations, microcracks, porosity, fiber breakage, and the simultaneous presence of these defects. Each defect is modeled as an additive variation in the material's electrical conductivity tensor, allowing for a detailed mathematical representation of the defect's influence on the CFRP's electromagnetic behavior. The additivity of the variations in the conductivity tensor is justified by the assumption that the defects are not visible to the naked eye, implying that the material does not require non-destructive testing. The adapted EC model admits a unique and stable solution by verifying that all analytical steps are satisfied. To reconstruct 2D maps of the magnetic flux density amplitude, a FEM formulation is adopted, based on the energy functional because it ensures a stable and consistent numerical formulation given its coercivity. Moreover, the numerical approach allows precise and reliable numerical solutions, enhancing the capability to detect and quantify defects. The numerical results show that the obtained 2D maps are entirely superimposable on those highlighting the distribution of mechanical stress states known in the literature, offering a clear advantage in terms of detection costs. This approach provides an effective and economical solution for the non-destructive inspection of CFRP, ensuring accurate and timely defect diagnosis for maintaining structural integrity.

Keywords: EC; defects in CFRP; electrical conductivity tensor; Lax–Milgram theorem; solution stability; 2D maps of magnetic flux density amplitude

MSC: 35Q61; 35Q74

check for updates

Citation: Versaci, M.; Laganà, F.; Morabito, F.C.; Palumbo, A.; Angiulli, G. Adaptation of an Eddy Current Model for Characterizing Subsurface Defects in CFRP Plates Using FEM Analysis Based on Energy Functional. *Mathematics* **2024**, *12*, 2854. https://doi.org/10.3390/math12182854

Academic Editor: Sheng-Wei Chi

Received: 2 August 2024
Revised: 4 September 2024
Accepted: 11 September 2024
Published: 13 September 2024

Copyright: © 2024 by the authors. Licensee MDPI, Basel, Switzerland. This article is an open access article distributed under the terms and conditions of the Creative Commons Attribution (CC BY) license (https://creativecommons.org/licenses/by/4.0/).

1. Introduction

Non-Destructive Testing (NDT) techniques encompass a set of tests and inspections carried out without destroying or removing samples from the specimen under examination, aimed at detecting and identifying defects and, if possible, assessing their extent [1,2]. NDT methodologies are varied, and each is suited, by its characteristics or type of instrumentation, to be used effectively in different situations depending on the product's characteristics to be analyzed [3]. Among these, liquid penetrant techniques and ultrasonic ones have found extensive use but have specific limitations. In particular, liquid penetrants, while effective for detecting surface discontinuities, struggle with reconstructing the shapes of defects, similar to ultrasonic techniques, despite their notable versatility [1–3].

Eddy Current (EC) analysis is a widely used non-destructive investigation technique for evaluating defects in conductive materials [4–8] with defects that alter its electrical conductivity [9]. Recently, a lot of interest in applying this methodology to advanced composite materials (which exhibit a certain degree of conductivity), such as Carbon Fiber Reinforced Polymer (CFRP) plates, has increased significantly due to the growing prevalence of these materials in various industrial domains [4,10–12]. The sectors show a strong interest in these approaches because they allow for assessing the health of CFRP components through cost-effective procedures [4,10,11].

The EC approach stands out for its versatility, allowing the detection of any inhomogeneity in the material through geometric, electrical, or magnetic variations [4,10–12]. By adapting the method to the specific case, it is possible to detect inhomogeneities related to the material's geometry, such as cracks, deformations, inclusions, thickness variations, oxidation, and thicknesses of non-conductive coatings on a conductive base or conductive coatings on a base of different conductivity, as well as variations in the material's permeability by measuring the intensity of magnetic fields. It is worth noting that a significant reason for the widespread use of EC is their ability to produce 2D maps, such as the modulus of the magnetic induction field, which are entirely superimposable on 2D maps representing the distribution of local mechanical stresses. This allows for detecting internal defects without needing expensive, non-portable machinery typical of mechanical stress measurement techniques [9,13–16]. Additionally, because EC is susceptible to the skin effect, the frequency of the external excitation current density produces a penetrative effect in the material, facilitating the production of 2D maps for each depth, depending on the type of defect to be detected [4,10,11,17].

Over the last decade, the aviation industry has also focused on this important NDT to improve aircraft safety, particularly after several takeoff/landing cycles, by combining low structural weight with high damage tolerance [18]. Consequently, new classes of CFRPs have been used, which are thermosetting materials incorporating carbon nanotube fibers, offering an exceptional combination of strength and lightness [18,19]. These materials are designed to withstand high loads while maintaining a lightweight structure for the aviation industry [18,19]. Although the production of CFRPs is expensive, their use is widely justified, where a high strength-to-weight ratio and significant resilience are indispensable requirements. The ability of CFRPs to maintain high structural integrity stressed and reduce the aircraft's overall weight significantly contributes to flight efficiency and safety [20].

Moreover, CFRPs offer excellent mechanical performance due to the strategic orientation of the carbon fibers within the polymer matrix, optimizing load distribution and increasing damage tolerance [20,21]. This characteristic is significant for resisting impacts and cyclic stresses during service. Additionally, the good corrosion resistance of CFRPs makes them suitable for operation in harsh environments, where exposure to moisture, chemicals, and other corrosive agents can compromise the durability and reliability of traditional materials [20,21].

However, CFRPs are susceptible to various types of defects (as mentioned above) that can compromise the material's quality by substantially changing the electrical conductivity of the material [22,23]. Among these, delamination is considered the most severe defect, but other significant defects such as microcracks, porosity, fiber breakage, and the simultaneous presence of these defects also impair the material's performance. Delamination in particular is a problem exacerbated by low off-axis electrical conductivity, which causes the material to heat up. The remarkable ability of these composites to absorb impact energy is another cause of delamination. Furthermore, the cycles of loading and unloading during flights do not prevent the onset of this dangerous phenomenon (in addition to the presence of other defects), which, if neglected, can lead to structural collapse [22,23].

Due to the anisotropic behavior of CFRP conductivity, conventional NDT techniques fail to detect defects in these composites quickly. However, only the major airlines possess the equipment and specialized technical staff to conduct EC tests, while other companies rely on specific software, generally based on the finite element method (FEM), to perform

these inspections [9,22,23]. From the perspective of EC, the problem of detecting the presence and extent of a defect translates into adequately formulating the variation in electrical conductivity within the material where the defect is present [24]. In other words, effective defect detection involves the ability to model how the defect affects the distribution of electrical conductivity within the material, requiring a local formulation of the conductivity tensor mathematically defined to represent the material's properties accurately. A defect alters the local electrical characteristics, causing a reduction in conductivity [9,24]. Therefore, to properly model the presence of the defect, it is necessary to introduce a decrement in the conductivity tensor that reflects the defect's effect. This variation must be precisely formulated to ensure that simulations and analyses conducted through EC techniques can accurately detect and quantify defects. Such an approach enables a detailed representation of the altered electrical properties of the material, facilitating the detection and assessment of the extent of defects.

Recently, many researchers have worked hard to provide innovative formulations of electrical conductivity and the possible variation that arises in the presence of defects. In particular, ref. [25] uses electrical impedance tomography to determine the electrical conductivity of anisotropic CFRP laminates and localize damage, while [26] presents a CFRP evaluation model using high-energy EC imaging frequency to detect critical defects that affect electrical conductivity. Furthermore, there is no shortage of work regarding coupled mechanical and electrical models in CFRPs [27,28], with particular reference to the distribution of EC in CFRPs and characterization of defects through the use of a tensor conductivity model [24,29–32].

In this paper, starting from [9], we characterize the subsurface defects (delamination, microcracks, porosity, fiber breaks, and their simultaneous presence) on CFRP tail rudders for civil aircraft using, for each of them is an innovative tensor formulation that locally models the lowering of electrical conductivity. In particular, unlike what was developed in [9], where we observe a focus on CFRPs used in civil aeronautics by introducing the use of fuzzy similarity for the classification and identification of sub-surface delamination, in this paper, we introduce a FEM analysis based on a complete mathematical formulation [33] of the EC on CFRP plates in which the conductivity tensor is altered by the presence of the defect which induces a local variation of the tensor itself. Unlike what was elaborated in [9], the analysis carried out is not limited exclusively to delaminations but rather to a wide range of defects that could occur simultaneously. From this, it follows that the 2D maps of the amplitude of the magnetic flux density, $|\mathbf{B}|$, are considerably more complete and completely superimposable (qualitatively) on the analogous 2D maps of mechanical tension (obtained from plates with the same types and extensions of defects) which, notoriously, are extremely difficult to obtain, often at very high costs [13,16]. These 2D maps of $|\mathbf{B}|$ represent a valid tool of classification and evaluation of the extent of each defect or the concomitance of them. Furthermore, unlike in [9], where the FEM approach was built directly from the model equations, in this paper, the numerical model was obtained starting from the energy functional associated with the weak form of the complete problem in which the presence of the defect updates the conductivity tensor. From this, being the energy functional coercive, and thanks to its stationary, the resulting numerical model was found to be stable. The resulting algebraic system, characterized by a positive definite but still sparse matrix, was solved using the conjugate gradient method with a Cholesky preconditioner. Furthermore, appropriate error estimates defined in appropriate functional spaces made obtaining a single sufficiently refined mesh capable of highlighting even the smallest defects possible.

Once the conductivity properties in CFRPs are defined in Section 2, Sections 3 and 4 detail each tensor formulation of the conductivity variation due to each hypothesized defect. Then, once the domain is defined in detail (Section 5), the complete EC model proposed in [33] is adapted in Sections 6 and 7 to our specific needs, also providing the necessary observations to certify the use. Therefore, starting from the weak formulation of the model (Section 8), the energy functional obtained allows us verification of the existence and uniqueness of the weak solution (Section 9), also guaranteeing stability (Section 10).

The FEM approach described in Section 11 produces a positive definite sparse matrix algebraic system whose resolution proposed in Section 12 allows the error to be estimated (Section 13). The following section offers an overview of the case studies considered, providing a convergence analysis helpful in building a unique mesh for any defect to obtain 2D maps of magnetic flux density valuable amplitude for the detection and evaluation of the entity of each defect or the concomitance between them. Finally, conclusions and some future perspectives end the paper.

2. Conductivity Properties of CFRP

Modeling fiber orientation and its effects is vital for designing CFRP components, optimizing performance for safety and efficiency. Therefore, let us consider two Cartesian axis systems, one original and one rotated, representing the fiber orientation in CFRP (Figure 1a). Indicating by Ω_C the domain of the CFRP (conductor), $\forall \mathbf{x} \in \Omega_C \subset \mathbb{R}^3$, in CFRP the base fiber orientation defines the conductivity tensor in the original configuration $\boldsymbol{\sigma}_0(\mathbf{x})$ as (in order not to burden the notation, the functional dependence on $\mathbf{x}$ is implied) [9,34–36]

$$\boldsymbol{\sigma}_0 = \begin{pmatrix} \sigma_{\parallel} & 0 & 0 \\ 0 & \sigma_{\perp} & 0 \\ 0 & 0 & \sigma_{\perp} \end{pmatrix} \tag{1}$$

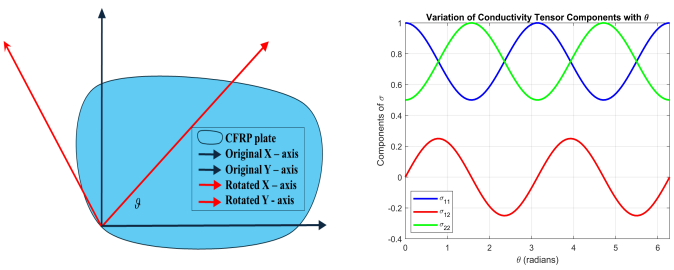
In (1), $\sigma_{\parallel}$ is the conductivity along the fibers, and $\sigma_{\perp}$ is the transverse conductivity. Locally, both are scalars, but their spatial distribution varies with fiber orientation, affecting the overall material properties. When the fiber orientation is rotated by angle θ relative to the reference axes (crucial for determining changes in anisotropic properties), the rotated conductivity tensor can be obtained using rotation matrix $\mathbf{R}(\theta)$. The rotation matrix in the xy plane, for a rotation by θ about the z axis, is given by

$$\mathbf{R}(\theta) = \begin{pmatrix} \cos\theta & -\sin\theta & 0 \\ \sin\theta & \cos\theta & 0 \\ 0 & 0 & 1 \end{pmatrix} \tag{2}$$

Thus, $\boldsymbol{\sigma}$ is then obtained by applying transformation

$$\boldsymbol{\sigma} = \mathbf{R}(\theta)\boldsymbol{\sigma}_0\mathbf{R}(\theta)^T = \begin{pmatrix} \sigma_{\parallel}\cos^2\theta + \sigma_{\perp}\sin^2\theta & (\sigma_{\parallel} - \sigma_{\perp})\cos\theta\sin\theta & 0 \\ (\sigma_{\parallel} - \sigma_{\perp})\cos\theta\sin\theta & \sigma_{\parallel}\sin^2\theta + \sigma_{\perp}\cos^2\theta & 0 \\ 0 & 0 & \sigma_{\perp} \end{pmatrix}, \tag{3}$$

which transforms $\boldsymbol{\sigma}_0$ to a rotated configuration, crucial for calculating property changes due to fiber orientation, highlighting the changes in anisotropic properties.



a **b**

Figure 1. (**a**) Relationship between the principal axes and the reference axes. (**b**) Dependence on θ of each element in (3).

Matrix (2) totally defines $\boldsymbol{\sigma}$ for an anisotropic material as a function of θ. Particularly, in it, $\sigma_{\parallel}\cos^2\theta + \sigma_{\perp}\sin^2\theta$, indicating the conductivity along the principal x direction after rotation and influenced by both $\sigma_{\parallel}$ and $\sigma_{\perp}$, modulated by the squares of the cosine and

sine functions of θ, reflecting the mixture of conductivities along and transverse to the fibers, varying with θ. Moreover, $(\sigma_{\parallel} - \sigma_{\perp}) \cos\theta \sin\theta$ in the off-diagonal positions manage the mixed conductivity between x and y directions due to the inclined fiber orientation, highlighting that the conductivity variation reaches its maximum at $\theta = 45^{\circ}$ and disappears when the fibers are aligned along one of the principal axes, at 0 or 90 degrees. Moreover, $\sigma_{\parallel} \sin^2\theta + \sigma_{\perp} \cos^2\theta$ corresponds to the conductivity in the y direction after rotation and, like its symmetric counterpart in the first row and column, combines the parallel and perpendicular conductivities influenced by the rotation angle. Finally, $\sigma_{\perp}$, locally, remains constant, suggesting that the conductivity in the z direction, perpendicular to the xy plane, is unaffected by the rotation in the xy plane. This assumes an isotropic behavior of transverse conductivity in the xy plane.

Figure 1b depicts the variation of the components of $\boldsymbol{\sigma}$ as function θ. The plot shows three components of $\boldsymbol{\sigma}$: σ_{11}, σ_{12}, and σ_{22}, which are represented by the blue, red, and green curves, respectively. As θ varies from 0 to 2π radians, σ_{11} (blue curve) and σ_{22} (green curve) exhibit a periodic behavior indicating that the longitudinal and transverse conductivities are dependent on the fiber orientation, showing maximum values when the fibers are aligned with the principal axes and minimum values when they are rotated by $\pi/2$ radians. σ_{12} (red curve), which represents the off-diagonal term of $\boldsymbol{\sigma}$, also varies periodically with θ and highlights the coupling between the longitudinal and transverse directions in the presence of rotation, which is a characteristic feature of anisotropic materials. However, for obvious computational reasons, in this paper, we consider $\theta = 0$ so that the direction of the fibers coincides with that of the x-axis.

Remark 1. *To be precise, when defects arise in CFRP, the reference frame should rotate in space, necessitating the use of a set of angles (e.g., Euler angles). However, it has been demonstrated that for typical CFRP used in commercial aircraft construction, the anisotropies resulting from rotations apart from θ can be considered negligible.*

3. Influence of Defects on Electrical Conductivity in CFRP: Some Physical–Mathematical Properties

As detailed above, the baseline conductivity in a CFRP can be described by $\boldsymbol{\sigma}$, which in ideal conditions (without defects) is primarily determined by the orientation and distribution of carbon fibers, $\boldsymbol{\sigma} = \boldsymbol{\sigma}(\theta, \boldsymbol{\sigma}_{\text{fiber}}, \boldsymbol{\sigma}_{\text{matrix}})$ where $\boldsymbol{\sigma}_{\text{fiber}}$, $\boldsymbol{\sigma}_{\text{matrix}}$ are the electrical conductivity of the carbon fibers within the CFRP and the electrical conductivity of the polymer matrix in which the carbon fibers are embedded. These fibers are oriented in specific directions, and their conductivity influences the overall anisotropic behavior of the material. The matrix typically has a much lower conductivity compared to the fibers and contributes to the transverse conductivity of the composite material [9,24]. Each type of defect alters $\boldsymbol{\sigma}$ in specific ways. Therefore, in this work, we modify $\boldsymbol{\sigma}$ as (the dependency on $\mathbf{x}$ and θ is implied) [37]

$$\boldsymbol{\sigma}' = \boldsymbol{\sigma} + \Delta\boldsymbol{\sigma}(\text{defect}) \tag{4}$$

where $\Delta\boldsymbol{\sigma}(\text{defects})$ represents the variation in the conductivity tensor due to a specific defect. Obviously, to ensure that $\Delta\boldsymbol{\sigma}$ correctly represents the defects in the material and that the resulting model is both mathematically and physically valid, it must satisfy the following properties. Firstly, $\Delta\boldsymbol{\sigma}(\text{defects})$ must be physically compatible, that is,

$$\boldsymbol{\sigma}' = \boldsymbol{\sigma} + \Delta\boldsymbol{\sigma}(\text{defect}) \geq 0, \quad \forall \mathbf{x} \in \Omega \tag{5}$$

with sufficient regularity ($\Delta\boldsymbol{\sigma}(\text{defect}) \in C^0(\Omega)$ or preferably $\Delta\boldsymbol{\sigma}(\text{defect}) \in C^1(\Omega)$). Furthermore, it must be able to localize defects: $\Delta\boldsymbol{\sigma}(\text{defect}) \neq 0$ only in regions with defects. Additionally, $\Delta\boldsymbol{\sigma}(\text{defect})$ must respect the isotropic or anisotropic properties of the material, ensuring boundedness.

Remark 2. *It is worth noting that in the local reference frame, $\Delta\boldsymbol{\sigma}$ is indeed a diagonal matrix because it represents the change in conductivity along the principal axes of the material, where the directions are aligned with the eigenvectors of the conductivity matrix. However, when a rotation is applied to the reference frame, the $\Delta\boldsymbol{\sigma}$ matrix becomes a full matrix. This occurs because the rotation mixes the components of conductivity along the different directions, introducing off-diagonal terms in the resulting matrix. In other words, after the rotation, the conductivity is no longer perfectly aligned with the original principal axes, leading to non-zero off-diagonal components in the transformed $\Delta\boldsymbol{\sigma}$ matrix. This process is imperative for accurately describing the anisotropy induced by defects in the material.*

4. Formulation of the Conductivity Tensor Variation as a Function of the Defect Type

In this section, we propose a detailed formulation for $\Delta\boldsymbol{\sigma}$ representing the variation in the conductivity tensor for each type of defect, including delamination, microcracks, porosity, fiber breakage, and combinations of these defects. This approach allows us to mathematically characterize the impact of each defect on the electrical properties of CFRP materials.

4.1. Formulation of the Conductivity Tensor Variation Due to Delamination

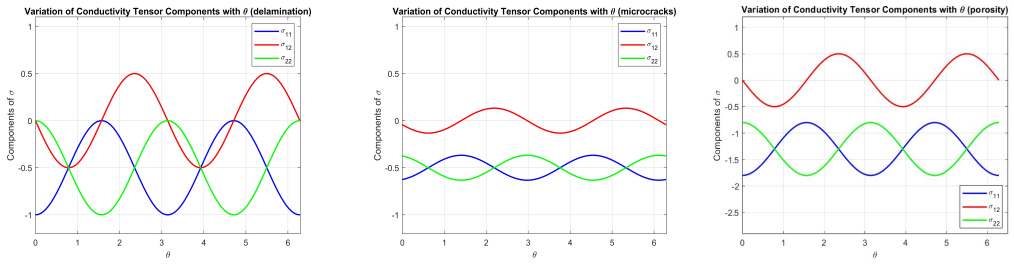
Delamination disrupts the continuity in CFRP, reducing its electrical conductivity. This phenomenon occurs due to separation between the laminate layers of the composite, which disrupts the continuous conductive paths, causing the overall electrical resistivity [9,37,38].

$\Delta\boldsymbol{\sigma}$ for delamination can be expressed as (for simplicity of notation, we consider the dependence on θ to be implicit) [37,38]

$$\Delta\boldsymbol{\sigma}_{\text{delamination}} = -\alpha\hat{n}\otimes\hat{n} = -\alpha\begin{pmatrix} n_1^2 & n_1n_2 & n_1n_3 \\ n_2n_1 & n_2^2 & n_2n_3 \\ n_3n_1 & n_3n_2 & n_3^2 \end{pmatrix}, \tag{6}$$

where $\hat{n} = (n_1, n_2, n_3)$ is the unit vector normal to the delamination surface and α is a parameter dependent on the extent and severity of the delamination. Since (6) is a symmetric tensor, it can be deduced that, along a θ direction, no anisotropic phenomena occur.

Figure 2a depicts the variation of the components of $\boldsymbol{\sigma}$ as a function of θ. In the presence of delamination, the oscillatory trend remains but with evident alterations in amplitude and baselines, introducing a marked anisotropy, reducing the overall conductivity and altering the distribution of the electric field within the material. σ_{11} and σ_{22} show a reduction in overall conductivity by interrupting the conductive paths provided by the carbon fibers (alteration between longitudinal and transverse directions).



a **b** **c**

Figure 2. Dependence on θ of each element in $\boldsymbol{\sigma}$ with (**a**) delamination, (**b**) microcracks, (**c**) porosity.

4.2. Formulation of the Conductivity Tensor Variation Due to Microcracks

Microcracks, introducing discontinuities along specific directions, decrease conductivity along the directions of the microcracks themselves by interrupting conductive paths and creating barriers to current flow. $\Delta\boldsymbol{\sigma}$, for microcracking, can be formulated as [39]

$$\Delta\boldsymbol{\sigma}_{\text{microcracks}} = -\beta \sum_k w_k (\mathbf{m}_k \otimes \mathbf{m}_k) = -\beta \sum_k w_k \begin{pmatrix} m_{k1}^2 & m_{k1}m_{k2} & m_{k1}m_{k3} \\ m_{k2}m_{k1} & m_{k2}^2 & m_{k2}m_{k3} \\ m_{k3}m_{k1} & m_{k3}m_{k2} & m_{k3}^2 \end{pmatrix} \tag{7}$$

where w_k represents the weight or relative influence of each group of microcracks oriented along $\mathbf{m}_k(\theta)$, and β quantifies the reduction in conductivity per unit area of microcracking (k, index identifying different groups of microcracks oriented in specific directions). $\mathbf{m}_k(\theta) \otimes \mathbf{m}_k(\theta)$ represents the influence of microcracks oriented along the direction $\mathbf{m}_k(\theta)$. It is easy to prove the regularity of (7); since $\mathbf{m}_k(\theta)$ and w_k are regular (because continuous and differentiable), then $\Delta\boldsymbol{\sigma}_{\text{microcracks}}(\theta)$ is also regular. Finally, we observe that microcracks, along a specific orientation θ, do not alter the anisotropy of the material since (7) is a symmetric tensor.

Figure 2b highlights the variation of the components of $\boldsymbol{\sigma}$ as a function of θ in the presence of microcracks. In particular, the trends, while maintaining sinusoidal trends, show a more limited reduction compared to delamination; furthermore, the baseline is slightly shifted due to a minor alteration of the coupling between the longitudinal and transversal directions [9,37,38].

4.3. Formulation of the Conductivity Tensor Variation Due to Porosity

Porosities in CFRP introduce voids in the material, reducing conductivity uniformly in all directions. To model $\Delta\boldsymbol{\sigma}$ due to porosity, we use the following formulation [9,37,38]:

$$\Delta\boldsymbol{\sigma}_{\text{porosity}} = -\gamma(1-p)\mathbf{I}, \tag{8}$$

where $(1-p)$ represents the percentage of non-porous material, while γ is a coefficient quantifying the effect of porosity on conductivity. Moreover, $\mathbf{I}$ is the identity matrix, indicating a uniform reduction in conductivity in all directions. Obviously, the regularity of (8) is ensured, since p and γ are continuous and differentiable. Moreover, since p varies spatially, $\Delta\boldsymbol{\sigma}_{\text{porosity}}$ reflects these variations, localizing the effect of porosity in the appropriate regions of the material. Finally, (8), for each θ, does not alter the material's anisotropy since $\mathbf{I}$ it is symmetric by definition.

As above, Figure 2c depicts the variation of the components of $\boldsymbol{\sigma}$ as a function of θ in the presence of porosity. Furthermore, in this case, while still maintaining the wave phenomenon (but with reduced amplitude compared to previous cases), a reduction in conductivity is observed due to the presence of voids in the material.

4.4. Formulation of the Conductivity Tensor Variation Due to Fiber Breakage

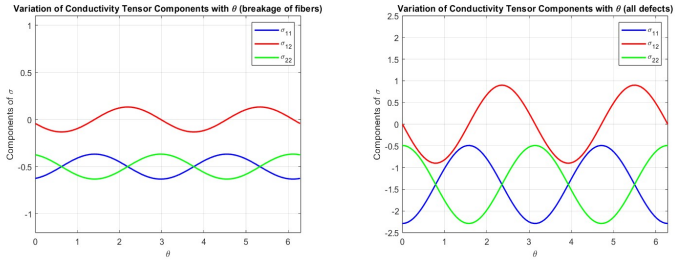
To model the variation of $\boldsymbol{\sigma}$ due to fiber breakage that directly affects the conductivity along the axis of the broken fibers, we exploit the following formulation [9,37,38]:

$$\Delta\boldsymbol{\sigma}_{\text{fiber breakage}} = -\delta\mathbf{f} \otimes \mathbf{f}. \tag{9}$$

In (9), δ quantifies the reduction in conductivity due to each broken fiber, while $\mathbf{f}$ describes the direction of a specific defect. The tensor product $\mathbf{f} \otimes \mathbf{f}$ represents the direction of the fiber and how conductivity is reduced along this direction. Obviously, (9) is regular because δ is a scalar. Moreover, since $\mathbf{f} \otimes \mathbf{f}$ is a symmetric tensor, (9) does not alter the material anisotropy for each θ.

Figure 3a shows how the breakage of fibers affects the components of $\boldsymbol{\sigma}$. Particularly, it is clear that, unlike other defects, the influence that the breakage of the fibers manifests in

terms of conductivity is considerably reduced. It follows that, on a hypothetical scale of risk of defects, the breakage of the fibers does not raise particular concerns.



a **b**

Figure 3. Dependence on θ of each element in $\boldsymbol{\sigma}$ with (**a**) breakage of fibers and (**b**) all defects.

4.5. Formulation of the Conductivity Tensor Variation When All Defects Act Simultaneously

For evaluating the overall impact of multiple types of defects on $\boldsymbol{\sigma}$, we combine all formulations into a unified model,

$$\Delta\boldsymbol{\sigma}_{\textbf{all defects}} = \Delta\boldsymbol{\sigma}_{\text{delamination}} + \Delta\boldsymbol{\sigma}_{\text{microcracks}} + \Delta\boldsymbol{\sigma}_{\text{porosity}} + \Delta\boldsymbol{\sigma}_{\text{fiber breakage}}. \tag{10}$$

Figure 3b plots $\Delta\boldsymbol{\sigma}_{\textbf{all defects}}$, from which it can be seen that the variation in conductivity in the material is extremely marked. Additive property (10) is based on the independence of effects, linearity of conductivity variations, and superposition of solutions. Furthermore, if each variation $\Delta\boldsymbol{\sigma}_{\text{defect}}$ is regular, the sum of these variations is also regular. Moreover, the sum of conductivity variations maintains the localization of defects. The sum of these terms does not alter this localization but simply superimposes the local effects. The symmetry of the resulting conductivity tensor is preserved by the sum of symmetric variations.

5. Description of the Domain

Let us consider a bounded connected open set $\Omega \subset \mathbb{R}^3$, with boundary $\partial\Omega$. The unit outward normal vector on $\partial\Omega$ is denoted by $\mathbf{n}$. We assume that $\overline{\Omega}$ is split into two parts, $\overline{\Omega} = \overline{\Omega_C} \cup \overline{\Omega_I}$, where Ω_C is our CFRP plate and Ω_I (a perfect insulator) represents the surrounding space. These are open disjoint subsets, such that $\overline{\Omega_C} \subset \Omega$ because the CFRP plate is immersed within a larger space, Ω, also including the surrounding area which acts as a perfect insulator, Ω_I. These two domains, Ω_C and Ω_I, are open and disjoint sets, and therefore non-superposable. Moreover, it makes sense to consider Ω_I as connected because it represents the continuous, uninterrupted space surrounding the plate, ensuring that there are no other obstacles or materials between the plate and its surroundings.

We also suppose that Ω_I is connected because it represents the continuous insulating space surrounding the CFRP plate. We denote by $\Gamma := \partial\Omega_I \cap \partial\Omega_C$ the interface between the two subdomains; note that, in the present situation, $\partial\Omega_C = \Gamma$ and $\partial\Omega_I = \Gamma \cup \partial\Omega$, which represents the common boundary between the two subdomains, clarifying that $\partial\Omega_C$ coincides with Γ and that the total boundary $\partial\Omega_I$ is constituted by the union of Γ and the rest of the boundary of Ω.

Moreover, we indicate by Γ_i, $i = 1, \ldots, p_\Gamma$ the connected components of Γ and by $(\partial\Omega)_t$, $t = 0, 1, \ldots, p_{\partial\Omega}$ the connected components of $\partial\Omega$ (in particular, we denote by $(\partial\Omega)_0$ the external one (useful for distinguishing the external boundary from the rest of the interfaces within the domain, especially when boundary conditions must be applied)).

The assumption that Γ and $\partial\Omega$ have multiple connected components arises from the fact that Ω_C can have multiple contact surfaces (sides and edges of the plate) which can be split into separate connected components, especially if the geometry of the plate or the arrangement of the insulator presents complexity or peculiarities.

In the following, we let $\mathbf{x} \in \Omega \subset \mathbf{R}^3$ be the spatial coordinate regarding a system of orthonormal Cartesian axes, $Oxyz$, integral with the plate whose origin O coincides

with the left base angle of the plate, while the x and y axes represent the positions of the predominant sides of the plate itself. We let t be the time variable.

6. The Proposed Eddy Current Model

6.1. Analysis Regime

As is known, in EC models, a permanent sinusoidal regime is used to analyze the response to harmonic AC signals at a constant angular frequency, $\omega \neq 0$. Then, all the fields involved (electric $\mathbf{E}$, magnetic $\mathbf{H}$, electric displacement $\mathbf{D}$, magnetic flux density $\mathbf{B}$), as well as the EC ($\mathbf{J}$, the excitation current density (probe coil), $\mathbf{J}_e$), oscillate sinusoidally at the same frequency. It follows that, in such regimes, $\frac{\partial \mathbf{D}(\mathbf{x},t)}{\partial t}$ is negligible, ignoring transient effects by focusing on constant harmonic oscillations. Therefore, it makes sense to assume for $\mathbf{E}$, $\mathbf{H}$ and $\mathbf{J}_e$, $Re[\mathbf{E}(\mathbf{x})e^{j\omega t}]$, $Re[\mathbf{H}(\mathbf{x})e^{j\omega t}]$, respectively. Likewise, $\mathbf{J}_e$ also takes on the same connotation ($Re[\mathbf{J}_e(\mathbf{x})e^{j\omega t}]$). Obviously, $e^{j\omega t} \neq 0$ disappears since it is present in all terms of the equations and can therefore be eliminated from the computation [40].

6.2. Two Important Constitutive Laws

If $\mu(\mathbf{x})$, i.e., the positive magnetic permeability, is a positive uniformly defined symmetric matrix with entries in $L^\infty(\Omega)$, it follows that $\mathbf{B} = \mu\mathbf{H}$. The assumption that all entries belong to $L^\infty(\Omega)$ is justified both by physical considerations (realistic materials have limited permeability) and by mathematical (stability and uniqueness of PDE solutions) and practical needs (accuracy in numerical approximations). This allows us to accurately model the electromagnetic behavior of the CFRP material within Ω.

The constitutive law reads $\mathbf{E}$ and $\mathbf{D}$ is $\mathbf{D} = \epsilon\mathbf{E}$, where, in a linear and isotropic material, electrical permittivity $\epsilon(\mathbf{x}) \in L^\infty(\Omega)$ (with the same motivation concerning the magnetic permeability), while in anisotropic materials such as CFRP plates, ϵ is a second-order tensor in which all entries $\epsilon_{ij} \in L^\infty(\Omega)$. Finally, $\mu(\mathbf{x})$ is a positive uniformly defined symmetric matrix with entries in $L^\infty(\Omega)$. Therefore, as specified above, it makes sense to write $Re[\mathbf{D}(\mathbf{x})e^{j\omega t}]$ and $Re[\mathbf{B}(\mathbf{x})e^{j\omega t}]$.

6.3. Ohm's Law

Since Ω_I is a perfect insulator, we require that $\boldsymbol{\sigma}(\mathbf{x})_{|\Omega_I} = 0$; moreover, considering (5), the generalized Ohm's law becomes

$$\mathbf{J} = \boldsymbol{\sigma}'(\mathbf{x})\mathbf{E} + \mathbf{J}_e \tag{11}$$

where $\mathbf{J}_e$, being the external current density, does not vanish in Ω_C. Then, it is the ω pulsation, through the skin effect, that manages the penetration depths for the analysis of defects.

6.4. Some Remarks on the Skin Effect

Applying an AC $\mathbf{J}_e$, $\mathbf{H}$ generated, produces flux lines mostly concentrated at the center of the coil. $\mathbf{H}$ penetrates nearby Ω_C, EC. These EC form a secondary $\mathbf{H}$ field that opposes the primary field, influencing the test coil's impedance, $\mathbf{Z}$. As EC increases, $\mathbf{Z}$ decreases. The presence of defects in the material impedes the flow of EC, increasing $\mathbf{Z}$ and reducing the secondary field. $\boldsymbol{\sigma}$ directly affects the penetration of EC into the material according to a well-known formulation (see [9]). Then, by increasing ω, the frequency, f, of the excitation current is increased, so the higher the f, the lower the penetration depth, and vice versa.

6.5. Boundary Conditions

In the case under study, the CFRP plate can be considered as a plate within a cavity surrounded by an infinitely permeable material. Therefore, we need to specify the boundary conditions for both $\mathbf{H}$ and $\mathbf{E}$. Concerning $\mathbf{H}$, for an infinitely permeable material, the tangential component of the magnetic field $\mathbf{H}$ vanishes on the boundary $\partial\Omega$, $\mathbf{H} \times \mathbf{n} = \mathbf{0}$, where $\mathbf{n}$ is the unit outward normal vector on $\partial\Omega$. This condition implies that $\mathbf{H}$ is perfectly

aligned with the boundary surface, which ensures that there is no tangential magnetic field component at the boundary. Next, concerning **E**, the tangential component of the electric field **E** also vanishes on $\partial\Omega$, $\mathbf{E} \times \mathbf{n} = \mathbf{0}$. This means that **E** must be perpendicular to the boundary surface, ensuring that there is no tangential electric field component at the boundary.

6.6. Some Additional Remarks on Ω

To guarantee the regularity of the solutions of the PDEs describing electromagnetic fields, it is necessary to assume that either $\partial\Omega \in C^{1,1}$ or Ω is a Lipschitz polyhedron. Condition $\partial\Omega \in C^{1,1}$ means that $\partial\Omega$ is differentiable with continuous first derivatives and bounded second derivatives. This ensures that the surfaces are smooth and free of irregularities. If Ω is a Lipschitz polyhedron, the boundaries are made up of flat segments, and this property greatly simplifies the formulation and solution of equations on the domain. For the CFRP plate (Ω_C), having a regular boundary or being a Lipschitz polyhedron ensures that the electromagnetic properties can be accurately calculated and that the interactions with the electromagnetic field are modeled correctly. Likewise, considering the surrounding space (Ω_I) with these properties ensures that boundary conditions and interfaces are treated rigorously and precisely. Consequently, as proved in [33,41], we need to consider the following spaces of harmonic vector fields:

$$\begin{aligned}\mathcal{H}_{\mu_I}(\partial\Omega;\Gamma) := \{\mathbf{v}_I \in (L^2(\Omega_I))^3 \mid \nabla \times \mathbf{v}_I = \mathbf{0},\ \nabla \cdot (\mu_I \mathbf{v}_I) = 0,\\ \mathbf{v}_I \times \mathbf{n} = \mathbf{0} \text{ on } \partial\Omega,\ \mu_I \mathbf{v}_I \cdot \mathbf{n}_I = 0 \ \text{ on } \Gamma\}\end{aligned} \tag{12}$$

and

$$\begin{aligned}\mathcal{H}_{\epsilon_I}(\Gamma;\partial\Omega) := \{\mathbf{v}_I \in (L^2(\Omega_I))^3 \mid \nabla \times \mathbf{v}_I = \mathbf{0},\ \nabla \cdot (\epsilon_I \mathbf{v}_I) = 0,\\ \mathbf{v} \times \mathbf{n}_I = \mathbf{0} \text{ on } \Gamma,\ \epsilon_I(\mathbf{x})\mathbf{v}_I \cdot \mathbf{n} = 0 \ \text{ on } \partial\Omega\}.\end{aligned} \tag{13}$$

Particularly, $\mathcal{H}_{\mu_I}(\partial\Omega;\Gamma)$ has a finite dimension equal to $p_{\partial\Omega} + n_\Gamma$, while the dimension of $\mathcal{H}_{\epsilon_I}(\Gamma;\partial\Omega)$, also finite, is equal to $p_\Gamma - 1 + n_{\partial\Omega}$. The following results hold [33].

Theorem 1. *There exist n_Γ cuts Ξ_l, which are the interiors of two-dimensional, mutually disjoint, compact, and connected Lipschitz manifolds $\overline{\Xi_l}$ with boundaries $\partial\Xi_l$, such that $\Xi \subset \Omega_I$ and $\partial\Xi_l \subset \Gamma$. In the open set $\widehat{\Omega_I} := \Omega_I \setminus \bigcup_l \Xi_l$, assumed to be connected, every curl-free vector field with vanishing tangential component on $\partial\Omega$ has a global potential.*

Remark 3. *Theorem 1 provides a condition for the existence of a global potential in the context of conservative vector fields in Ω_I (insulating space surrounding the CFRP plate), ensuring that an irrotational vector field, with zero tangential component on $\partial\Omega$, can be described by a global potential in the context of CFRP plates. In other terms, this theorem guarantees that the electric and magnetic fields within Ω_I interacting with the conductive CFRP material can be consistently described by potential functions. This enables precise modeling of the electromagnetic behavior within the CFRP plate, ensuring that the boundary conditions are met and the fields retain their physical significance.*

Theorem 2. *There exist $n_{\partial\Omega}$ cuts Σ_k, which are the interiors of two-dimensional, mutually disjoint, compact, and connected Lipschitz manifolds $\overline{\Sigma_k}$ with boundaries $\partial\Sigma_k$. In the open set $\widetilde{\Omega_I} := \Omega_I \setminus \bigcup_k \Sigma_k$, assumed to be connected, every curl-free vector field with vanishing tangential component on Γ has a global potential.*

Remark 4. *According to Theorem 2, the cuts within Ω_I ensure that the extended domain $\widetilde{\Omega_I}$ remains connected, which is essential for the existence of a global potential for irrotational vector fields. This connection in $\widetilde{\Omega_I}$ ensures that both the electric and magnetic fields can be described consistently and continuously around the CFRP plate. This is particularly important as it guarantees*

that the electromagnetic behavior in the insulating space surrounding the conductive plate is accurately modeled, maintaining the physical integrity of the fields and ensuring that they meet the required boundary conditions. This allows for a precise description of the interactions between the electric and magnetic fields and the CFRP material.

In particular, n_Γ represents the number of singular (or non-bounding) cycles in $\overline{\Omega_I}$ of the first type. These are cycles on Γ that cannot be represented as $\partial S \setminus \gamma$, where S is a surface contained in Ω_I and γ is a cycle, possibly empty, contained in $\partial\Omega$. Similarly, $n_{\partial\Omega}$ denotes the number of singular cycles in $\overline{\Omega_I}$ of the second type. These are cycles on $\partial\Omega$ that cannot be represented as $\partial S \setminus \gamma$, where S is a surface contained in Ω_I and γ is a cycle, possibly empty, contained in Γ.

In the context where Ω_C is the CFRP plate and Ω_I is the surrounding space, these definitions are particularly relevant. The first types of cycles, represented by n_Γ, involve the interactions at the interface Γ between the plate and the insulating space. These cycles reflect the complex geometries and potential discontinuities that can exist at the boundary of the CFRP plate. The second types of cycles, represented by $n_{\partial\Omega}$, pertain to the boundaries of the entire domain Ω. These cycles are essential for understanding the global topological constraints and ensuring that the fields have appropriate potentials in the context of the entire system, including both the plate and the surrounding space.

6.7. Necessary Conditions for External Current Density and Basis Functions

Let us assume that the external current density $\mathbf{J}_e \in (L^2(\Omega))^3$ satisfies the necessary conditions:

$$\begin{cases} \nabla \cdot \mathbf{J}_{e,I} = 0 \quad \text{in } \Omega_I, \\ \mathbf{J}_{e,I} \cdot \mathbf{n} = 0 \quad \text{on } \partial\Omega, \\ \int_{\Gamma_i} \mathbf{J}_{e,I} \cdot \mathbf{n}_I d\Gamma_i = 0 \quad \forall i = 1, \ldots, p_\Gamma - 1, \\ \int_{\Omega_I} \mathbf{J}_{e,I} \cdot \boldsymbol{\pi}_{k,I} d\Omega_I = 0 \quad \forall k = 1, \ldots, n_{\partial\Omega}, \end{cases} \tag{14}$$

where $\boldsymbol{\pi}_{k,I}$ are the basis functions of space $\mathcal{H}_{\epsilon_I}(\Gamma; \partial\Omega)$ that are not gradients. These conditions are necessary for the following reasons. Firstly, $\mathbf{J}_e \in (L^2(\Omega))^3$ guarantees that $\mathbf{J}_e$ is square-integrable over Ω to ensure that the current density has finite energy (essential for the physical realism and well posedness of the problem). Moreover, $\nabla \cdot \mathbf{J}_{e,I} = 0$ in Ω_I ensures that the external current density is curl-free in the insulating region. This is because in the absence of sources or sinks, the external current must form closed loops or be uniform. Furthermore, $\mathbf{J}_{e,I} \cdot \mathbf{n} = 0$ as $\partial\Omega$ ensures that there is no normal component of the external current density on the boundary, which aligns with the physical scenario where the current flows parallel to the surface of the CFRP plate. In addition, $\int_{\Gamma_j} \mathbf{J}_{e,I} \cdot \mathbf{n}_j d\Gamma_i = 0$ for all $j = 1, \ldots, p_\Gamma - 1$ ensures that the total applied current through each cut Σ_k is zero. This is necessary considering the Ampere law, since $\mathbf{H} \times \mathbf{n}$ vanishes on $\partial\Omega$ and hence on $\partial\Sigma_k$. Finally, $\int_{\Omega_I} \mathbf{J}_{e,I} \cdot \boldsymbol{\pi}_{k,I} d\Omega_I = 0$ for all $k = 1, \ldots, n_{\partial\Omega}$, involves basis functions $\boldsymbol{\pi}_{k,I}$ of space $\mathcal{H}_{\epsilon_I}(\Gamma; \partial\Omega)$ that are not gradients. This condition ensures that the external current density is orthogonal to these basis functions, facilitating the existence of a unique potential.

6.8. Complete System of Equations for the EC Problem

The following assertion is valid.

Proposition 1. *$\boldsymbol{\sigma}'$ is both symmetric and positive definite.*

Proof. We first observe that $\boldsymbol{\sigma}'$ is symmetric, $(\boldsymbol{\sigma}')^T = (\boldsymbol{\sigma} + \Delta\boldsymbol{\sigma})^T = (\boldsymbol{\sigma})^T + (\Delta\boldsymbol{\sigma})^T = \boldsymbol{\sigma} + \Delta\boldsymbol{\sigma} = \boldsymbol{\sigma}'$. Furthermore, $\Delta\boldsymbol{\sigma}$ being a small perturbation with respect to $\boldsymbol{\sigma}$, it follows that $\forall \mathbf{x} \in \mathbb{R}^n$, $\mathbf{x}^T \Delta\boldsymbol{\sigma} \mathbf{x}$ is sufficiently small compared to $\mathbf{x}^T \boldsymbol{\sigma} \mathbf{x}$. Therefore,

$$\mathbf{x}^T \boldsymbol{\sigma}' \mathbf{x} = \mathbf{x}^T (\boldsymbol{\sigma} + \Delta\boldsymbol{\sigma}) \mathbf{x} = \mathbf{x}^T (\boldsymbol{\sigma}\mathbf{x} + \Delta\boldsymbol{\sigma}\mathbf{x}) = \mathbf{x}^T \boldsymbol{\sigma}\mathbf{x} + \mathbf{x}^T \Delta\boldsymbol{\sigma}\mathbf{x} \approx \mathbf{x}^T \boldsymbol{\sigma}\mathbf{x}. \tag{15}$$

Therefore, $\boldsymbol{\sigma}$ being positive definite, $\boldsymbol{\sigma}'$ is also positive definite. □

Therefore, the complete system of equations describing the EC problem in terms of $\mathbf{H}$ and $\mathbf{E}_C$, proposed in [33], can be considered:

$$\begin{cases} \nabla \times \mathbf{E}_C + j\omega\mu_C\mathbf{H}_C = \mathbf{0}, \quad \text{in } \Omega_C \\ \nabla \times \mathbf{H}_C - \boldsymbol{\sigma}'\mathbf{E}_C = \mathbf{J}_{e,C}, \quad in \ \Omega_C \\ \nabla \times \mathbf{H}_I = \mathbf{J}_{e,I}, \quad \nabla \cdot (\mu_I\mathbf{H}_I) = 0 \quad \text{in } \Omega_I \\ \int_{(\partial\Omega)_t} \mu_I\mathbf{H}_I \cdot \mathbf{n} d(\partial\Omega)_t = 0 \quad \forall t = 1, \ldots, p_{\partial\Omega} \\ \int_{\Omega_I} j\omega\mu_I \cdot \boldsymbol{\rho}_{l,I} d\Omega_I + \int_\Gamma (\mathbf{E}_C \times \mathbf{n}_C) \cdot \boldsymbol{\rho}_{l,I} d\Gamma = 0, \quad \forall l = 1, \ldots, n_\Gamma \\ \mathbf{H}_I \times \mathbf{n} = \mathbf{0}, \quad \text{on } \partial\Omega \\ \mu_I\mathbf{H}_I \cdot \mathbf{n}_I + \mu_C\mathbf{H}_C \cdot \mathbf{n}_C = 0 \quad \text{on } \Gamma \\ \mathbf{H}_I \times \mathbf{n}_I + \mathbf{H}_C \times \mathbf{n}_C = \mathbf{0}, \quad \text{on } \Gamma, \end{cases} \tag{16}$$

in which $\boldsymbol{\sigma}$ is replaced by $\boldsymbol{\sigma}'$, since the required properties for $\boldsymbol{\sigma}'$ are inherited from $\boldsymbol{\sigma}$, as proved in Proposition 1.

In (16), for ensuring a consistent definition of the unit outward normal vectors, $\mathbf{n}_C = -\mathbf{n}_I$ on $\partial\Omega = \Gamma$. Furthermore, across Γ between the CFRP plate (Ω_C) and the surrounding space (Ω_I), $\mathbf{E}_C := \mathbf{E}_{|\Omega_C}$, $\mathbf{E}_I := \mathbf{E}_{|\Omega_I}$, $\mathbf{H}_C := \mathbf{H}_{|\Omega_C}$ and $\mathbf{H}_I := \mathbf{H}_{|\Omega_I}$.

Moreover, $\boldsymbol{\rho}_{l,I}$ represent the basis functions associated with the space of harmonic vector fields (12) that are not gradients.

It is worth noting that in [33], it has been proven that under the assumptions detailed above, Problem (16) has a unique solution when $\boldsymbol{\sigma}$ is considered.

In this paper, as usual, we consider (16) in terms of the Coulomb-gauged vector potential formulation, specifying that it is a well-posed formulation. These choices are appropriate for our CFRP problem, as they ensure the accurate modeling of electromagnetic fields in the complex structure of the CFRP plate and the surrounding space. By using the Coulomb gauge, we simplify the mathematical formulation and maintain the physical accuracy required for analyzing eddy currents in the CFRP material. It is important to introduce a gauge in the solution of $\mathbf{A}$ to ensure that the divergence-free condition, $\nabla \cdot \mathbf{A} = 0$, is satisfied. This condition is imperative because it ensures that the computed magnetic field is physically consistent and free from spurious sources. However, at low frequencies, the system of Maxwell equations tends not to naturally enforce this condition, which can lead to ill-conditioned or physically incorrect solutions. Introducing a gauge, such as the Lorenz condition, allows for control and correction of the behavior of the vector potential $\mathbf{A}$, ensuring that the solution remains consistent even in these particular cases. This guarantees that the formulation remains valid and accurate regardless of the frequency of the electromagnetic field under consideration.

Remark 5. *We note that Problem* (16) *admits only one solution when considering* $\boldsymbol{\sigma}'$*, at least when domain* Ω *and* Ω_C *has rather simple geometries. Furthermore, assuming that the EC problem is solvable in terms of* $\mathbf{E}_C$ *and* $\mathbf{H}$ *[33], the correct gauging conditions for the existence and uniqueness of the potential can be determined to include magnetic vector* $\mathbf{A}$ *and scalar electric potential* ϕ_C*. However, it is necessary to reformulate the problem in terms of vector potential and scalar to improve the accuracy and handling of boundary conditions by reducing the number of equations and variables.*

7. The Proposed Eddy Current Model: $(\mathbf{A}_C, \phi_C) - \mathbf{A}_I$ Formulation

7.1. Vector and Scalar Potential Formulation for the Magnetic and Electric Fields in CFRP and Surrounding Space

We seek magnetic vector potential $\mathbf{A}$ and scalar potential ϕ_C, such that in the CFRP plate, $\mathbf{B}_C$ can be expressed by $\mathbf{A}_C$, $\mu_C\mathbf{H}_C = \nabla \times \mathbf{A}_C$, where μ_C is the magnetic permittivity of Ω_C. Therefore, $\mathbf{E}_C$ becomes

$$\mathbf{E}_C = -j\omega\mathbf{A}_C - j\omega\nabla\phi_C, \tag{17}$$

from which, applying $\nabla\times$ to both sides, we obtain $\nabla \times \mathbf{E}_C = -j\omega\nabla \times \mathbf{A}_C = -j\omega\mu_C\mathbf{H}_C$, so that the Faraday equation is satisfied in Ω_C. Additionally, for Ω_I, it is appropriate to express $\mu_I\mathbf{H}_I$ as $\nabla \times \mathbf{A}_I$, where $\mu_I\mathbf{H}_I$ is a solenoidal field in Ω_I and has zero flux through any closed surface in $\overline{\Omega_I}$. In the case of the CFRP plate, this implies that the magnetic field in the surrounding space behaves as a solenoidal field, meaning it is divergence-free and the net magnetic flux through any closed surface is zero.

7.2. Matching Conditions and Coulomb Gauge

To guarantee the continuity and coherence of the electromagnetic fields across the interface between Ω_C and Ω_I, we need to formulate appropriate matching conditions. They ensure that the tangential and normal components of the potentials are coherent across Ω, avoiding unrealistic discontinuities. Condition

$$\mathbf{A}_I \times \mathbf{n}_I + \mathbf{A}_C \times \mathbf{n}_C = \mathbf{0} \quad \text{on } \Gamma, \tag{18}$$

ensures that the tangential components of the vector potential are continuous Γ (essential for the continuity of $\mathbf{H}$ through Γ). The imposition of the Coulomb gauge, $\nabla \cdot \mathbf{A} = 0$, simplifies equations and helps eliminate ambiguities in vector potentials. Furthermore, $\mathbf{A} \cdot \mathbf{n} = 0$ on $\partial\Omega$ completes the gauge definition and ensures that the vector potential is well defined over the entire domain.

Therefore, applying the Coulomb gauge to (18), we obtain $(\nabla \times \mathbf{A}_I) \cdot \mathbf{n}_I + (\nabla \times \mathbf{A}_C) \cdot \mathbf{n} = 0$ on Γ. This condition maintains physical consistency, preventing abrupt changes or discontinuities at the boundary. This is crucial for accurately modeling electromagnetic interactions and satisfying Maxwell equations. Furthermore, we also impose the following additional matching condition, $\mathbf{A}_I \cdot \mathbf{n}_I + \mathbf{A}_C \cdot \mathbf{n}_C = 0$, on Γ to ensure the continuity of the normal components of the vector potential across Γ.

Remark 6. *In a general geometric setting, this condition alone may not be sufficient to uniquely determine vector potential* $\mathbf{A}$ *in* Ω*. This is because there can exist non-trivial, irrotational, solenoidal, and tangential vector fields. These fields are elements of the finite-dimensional space of harmonic fields, defined as [33]*

$$\mathcal{H}(m;\Omega) := \{\mathbf{v} \in (L^2(\Omega))^3 \mid \nabla \times \mathbf{v} = \mathbf{0},\ \nabla \cdot \mathbf{v} = 0,\ \mathbf{v} \cdot \mathbf{n} = 0 \text{ on } \partial\Omega\}. \tag{19}$$

The existence of such fields indicates that additional conditions are required to ensure a unique solution for vector potential $\mathbf{A}$*. These harmonic fields are orthogonal to the gradients and capture the degrees of freedom that are not fixed by the previous conditions. Imposing these additional constraints is crucial for accurately modeling the electromagnetic interactions in complex geometries, ensuring that the solution for* $\mathbf{A}$ *is both unique and physically meaningful.*

Concerning space (19), to ensure that $\tilde{\Omega}$ remains connected and that every curl-free vector field within this space has a global potential, we are allowed to introduce the following Theorem [33].

Theorem 3. *Let* $n^*_{\partial\Omega}$ *denote the dimension of vector space* (19)*. There exist* $n^*_{\partial\Omega}$ *cuts* Σ^*_z*, which are the interiors of two-dimensional, mutually disjoint, compact, and connected Lipschitz manifolds* $\overline{\Sigma^*_z}$ *with boundaries* $\partial\Sigma^*_z$*. These cuts are such that* $\Sigma^*_z \subset \Omega$ *and* $\partial\Sigma^*_z \subset \partial\Omega$*, and in the open set* $\tilde{\Omega} := \Omega \setminus \cup\Sigma^*_z$*, assumed to be connected, every curl-free vector field has a global potential. In other words, each surface* Σ^*_z*,* $z = 1, \ldots, n^*_{\partial\Omega}$*, intersects a cycle on* $\partial\Omega$ *that does not bound a surface contained within* Ω*.*

The application of Theorem 3 uniquely determines $\mathbf{A}$ in Ω. Furthermore, Σ^*_z effectively break non-bounding loops on $\partial\Omega$, eliminating any topological impediments that prevent the existence of a unique global potential. This allows for a consistent and unique solution for $\mathbf{A}$.

7.3. Additional Conditions for Determining Unique Solutions in the Potential Formulation

In this context, we can specify the additional conditions that need to be imposed. Returning to the family of $n_{\partial\Omega}$ cuts Σ_k, we assume that the family of cuts Σ_z^* coincides with the family of cuts Σ_k for $z, k = 1, \ldots, n_{\partial\Omega}$ (specifically, $\Sigma_z^* \subset \Omega_I$ for each $z = 1, \ldots, n_{\partial\Omega}$), while $\Sigma_z^* \cap \Omega_C \neq \emptyset$ for each $z = n_{\partial\Omega} + 1, \ldots, n_{\partial\Omega}^*$. As a result, we have $n_{\partial\Omega} \leq n_{\partial\Omega}^*$.

When $n_{\partial\Omega} = n_{\partial\Omega}^*$, it indicates that we can select the cuts in Ω associated with vector space (19) without intersecting Ω_C. For instance, this occurs when Ω and Ω_C are two coaxial tori, where $n_{\partial\Omega} = 0$ and $n_{\partial\Omega}^* = 1$. In [33], it was shown that the number of additional conditions required,

$$\mathcal{G}_k(\mathbf{A}) = 0 \quad \forall k = 1, \ldots, n_{\partial\Omega}, \tag{20}$$

to be imposed on vector field $\mathbf{A}(\mathbf{x}, t)$m, is $n_{\partial\Omega}$. Finally, to find a unique solution $(\mathbf{A}_C, \phi_C)) - \mathbf{A}_I$, we impose the following condition for ϕ_C: $\int_{\Omega_{C,i}} \phi_{C|\Omega_{C,i}} d\Omega_{C,i} = 0$, where $\Omega_{C,i}$, $i = 1, \ldots, p_\Gamma$ are the connected components of Ω_C. These additional conditions are essential for ensuring that the vector potential $\mathbf{A}$ and the scalar potential ϕ_C are uniquely determined. Cuts Σ_z^* help in managing the topological constraints of the domain, ensuring that the electromagnetic fields can be accurately modeled without ambiguities. This is crucial for the precise analysis and detection of defects in CFRP plates using eddy current techniques, as it allows for a consistent and unambiguous representation of the electromagnetic interactions within the material and its surroundings.

7.4. Reformulated EC Model with Coulomb Gauge and Interface Conditions

Then, starting from the EC model (16) and considering what we just presented, the EC model formulated with Coulomb gauge and interface conditions takes the following form:

$$\begin{cases} \nabla \times \left(\frac{1}{\mu_C} \nabla \times \mathbf{A}_C \right) + j\omega \boldsymbol{\sigma}' \mathbf{A}_C + j\omega \boldsymbol{\sigma}' \nabla \phi_C = \mathbf{J}_{e,C} \quad \text{in } \Omega_C \\ \nabla \times \left(\frac{1}{\mu_I} \nabla \times \mathbf{A}_I \right) = \mathbf{J}_{e,I} \quad \text{in } \Omega_I \\ \int_{\Omega_{C,i}} \phi_{C|\Omega_{C,i}} d\Omega_{C,i} = 0 \quad \forall i = 1, \ldots, p_\Gamma \\ \nabla \cdot \mathbf{A}_C = 0 \quad \text{in } \Omega_C; \qquad \nabla \cdot \mathbf{A}_I = 0 \quad \text{in } \Omega_I \\ \mathcal{G}_k(\mathbf{A}) = 0 \quad \forall k = 1, \ldots, n_{\partial\Omega} \\ \mathbf{A}_I \cdot \mathbf{n} = 0, \quad \left(\frac{1}{\mu_I} \nabla \times \mathbf{A}_I \right) \times \mathbf{n} = 0 \quad \text{on } \partial\Omega \\ \mathbf{A}_I \cdot \mathbf{n}_I + \mathbf{A}_C \cdot \mathbf{n}_C = 0; \qquad \mathbf{A}_I \times \mathbf{n}_I + \mathbf{A}_C \times \mathbf{n}_C = \mathbf{0} \; on \; \Gamma \\ \left(\frac{1}{\mu_I} \nabla \times \mathbf{A}_I \right) \times \mathbf{n}_I + \left(\frac{1}{\mu_C} \nabla \times \mathbf{A}_C \right) \times \mathbf{n}_C = \mathbf{0} \quad on \; \Gamma. \end{cases} \tag{21}$$

As it is well established [41], $\nabla \cdot \mathbf{A} = 0$ in Ω can be integrated into the Ampere equation. By introducing the constant $\mu_* > 0$, which represents an appropriate average of the entries of μ in Ω, we consider the following formulation:

$$\begin{cases} \nabla \times \left(\frac{1}{\mu_C} \nabla \times \mathbf{A}_C \right) - \frac{1}{\mu_*} \nabla (\nabla \cdot \mathbf{A}_C) + j\omega \boldsymbol{\sigma}' \mathbf{A}_C + j\omega \boldsymbol{\sigma}' \nabla \phi_C = \mathbf{J}_{e,C} \quad \text{in } \Omega_C \\ \nabla \times \left(\frac{1}{\mu_I} \nabla \times \mathbf{A}_I \right) - \frac{1}{\mu_*} \nabla (\nabla \cdot \mathbf{A}_I) = \mathbf{J}_{e,I} \qquad \in \quad \Omega_I \\ \nabla \cdot (j\omega \boldsymbol{\sigma}' \mathbf{A}_C + j\omega \boldsymbol{\sigma}' \nabla \phi_C) = \nabla \cdot \mathbf{J}_{e,C} \quad \text{in } \Omega_C \\ (j\omega \boldsymbol{\sigma}' \mathbf{A}_C + j\omega \boldsymbol{\sigma}' \nabla \phi_C) \cdot \mathbf{n}_C = \mathbf{J}_{e,C} \cdot \mathbf{n}_C + \mathbf{J}_{e,I} \cdot \mathbf{n}_I \quad \text{on } \Gamma, \end{cases} \tag{22}$$

However, in (22), the last two conditions being necessary as the modification in the first two does not assure now that electric field (17) satisfies the following two necessary

conditions: $\nabla \cdot (\boldsymbol{\sigma}' \mathbf{E}_C) = -\nabla \cdot \mathbf{J}_{e,C}$ in Ω_C, and $\boldsymbol{\sigma}' \mathbf{E}_C \cdot \mathbf{n}_C = -\mathbf{J}_{e,C} \cdot \mathbf{n}_C - \mathbf{J}_{e,I} \cdot \mathbf{n}_I$ on Γ. Therefore, the complete EC model becomes

$$\begin{cases} \nabla \times \left(\frac{1}{\mu_C} \nabla \times \mathbf{A}_C \right) - \frac{1}{\mu_*} \nabla (\nabla \cdot \mathbf{A}_C) + j\omega \boldsymbol{\sigma}' \mathbf{A}_C + j\omega \boldsymbol{\sigma}' \nabla \phi_C = \mathbf{J}_{e,C} \quad \text{in } \Omega_C \\ \nabla \times \left(\frac{1}{\mu_I} \nabla \times \mathbf{A}_I \right) - \frac{1}{\mu_*} \nabla (\nabla \cdot \mathbf{A}_I) = \mathbf{J}_{e,I} \qquad \text{in } \Omega_I \\ \nabla \cdot (j\omega \boldsymbol{\sigma}' \mathbf{A}_C + j\omega \boldsymbol{\sigma}' \nabla \phi_C) = \nabla \cdot \mathbf{J}_{e,C} \quad \text{in } \Omega_C \\ (j\omega \boldsymbol{\sigma}' \mathbf{A}_C + j\omega \boldsymbol{\sigma}' \nabla \phi_C) \cdot \mathbf{n}_C = \mathbf{J}_{e,C} \cdot \mathbf{n}_C + \mathbf{J}_{e,I} \cdot \mathbf{n}_I \quad \text{on } \Gamma \\ \int_{\Omega_{C,i}} \phi_{C|\Omega_{C,i}} d\Omega_{C,i} = 0 \quad \forall i = 1, \ldots, p_\Gamma \\ \mathcal{G}_k(\mathbf{A}) = 0 \quad \forall k = 1, \ldots, n_{\partial\Omega} \\ \mathbf{A}_I \cdot \mathbf{n} = 0 \qquad \text{on } \partial\Omega \\ \left(\frac{1}{\mu_I} \nabla \times \mathbf{A}_I \right) \times \mathbf{n} = 0 \qquad \text{on } \partial\Omega \\ \nabla \cdot \mathbf{A}_I - \nabla \cdot \mathbf{A}_C = 0, \quad \mathbf{A}_I \cdot \mathbf{n}_I + \mathbf{A}_C \cdot \mathbf{n}_C = 0 \quad \mathbf{A}_I \times \mathbf{n}_I + \mathbf{A}_C \times \mathbf{n}_C = \mathbf{0}, \quad \text{on } \Gamma \\ \left(\frac{1}{\mu_I} \nabla \times \mathbf{A}_I \right) \times \mathbf{n}_I + \left(\frac{1}{\mu_C} \nabla \times \mathbf{A}_C \right) \times \mathbf{n}_C = \mathbf{0} \qquad \text{on } \Gamma. \end{cases} \tag{23}$$

The interface condition $\nabla \cdot \mathbf{A}_I = \nabla \cdot \mathbf{A}_C$ on Γ is necessary to assure that for a solution to (23), one has $\nabla \cdot \mathbf{A} = 0$ in the whole Ω, and therefore one can recover from (23) the original system (21). The Lemma 2.1 in [33] proves this assertion.

8. Weak Formulation and Energy Functional for the EC Problem

The rule that the vector field must have both a well-defined and integrable curl and divergence is crucial for writing the weak formulation of an EC problem, especially when dealing with CFRP plates. This arises from the complex behavior of composite materials and the nature of the non-destructive analysis techniques used to detect defects. In particular, $\Delta\boldsymbol{\sigma}$, due to the presence of defects, significantly affects the local distribution of currents within the material, altering the distribution of $\mathbf{H}$ and $\mathbf{E}$. It is known that $\nabla\cdot$ measures how much a field tends to expand or contract at a point, while $\nabla\times$ measures how much the field tends to rotate around a point. Having both the divergence and the rotor well defined and integrable ensures that the behavior can be accurately described throughout Ω. The weak formulation allows these fields to be considered in a more general and less restrictive context, allowing the problem to be solved even in the presence of irregularities in the material.

Therefore, as in [33], we are preliminarily considering the following functional spaces:

$$H(\text{curl}; \Omega) := \{\mathbf{v} \in (L^2(\Omega))^3 \mid \nabla \times \mathbf{v} \in (L^2(\Omega))^3\}, \tag{24}$$

and

$$H(\text{div}; \Omega) := \{\mathbf{v} \in (L^2(\Omega))^3 \mid \nabla \cdot \mathbf{v} \in L^2(\Omega)\}, \tag{25}$$

in order the test function $\mathbf{v}$, together, both $\nabla \times \mathbf{v}$ and $\nabla \cdot \mathbf{v}$ are square-integrable in Ω.

Remark 7. *In the case of CFRP plates, the request that curl and toe-out be quadratic-integrable, rather than simply module-integrable, is important for several reasons. Firstly, quadratic integrability ensures that local variations of $\boldsymbol{\sigma}$ are correctly captured without introducing non-physically realistic singularities or discontinuities. Furthermore, since both operators appear in the energy functional, quadratic integrability ensures that the system has finite energy. In other words, if we observe the problem from the perspective of signal theory, the definition of energy of any signal always imposes quadratic integrability. Then, spaces (24) and (25) are chosen because they naturally include the quadratic integrability condition for the vector field and its derivatives (rotor and*

divergence). Using these spaces allows exploitation of consolidated mathematical properties that facilitate the analysis and resolution of the problem. Finally, as is known, quadratic integrability ensures that numerical solutions are stable and convergent (if we only required module integrability, we could have solutions that do not converge or that present numerical instabilities, making the analysis less reliable). Therefore, $\mathbf{v} \in H(curl;\Omega) \cap H(div;\Omega)$*, with* $\mathbf{v}\cdot\mathbf{n} = 0$ *on* $\partial\Omega$*.*

To obtain the weak formulation, qw multiply its first equation by the complex conjugate of $\mathbf{v}_C$, $\overline{\mathbf{v}_C}$, and its second equation for the complex conjugate of $\mathbf{v_I}$, $\overline{\mathbf{v}_I}$. Therefore, it integrates over Ω. Next, the well-known rule of integration by parts is applied to easily obtain [33]

$$\int_{\Omega_C}\left(\frac{1}{\mu_C}(\nabla\times\mathbf{A}_C)\cdot(\nabla\times\overline{\mathbf{v}_C})+\frac{1}{\mu_*}(\nabla\cdot\mathbf{A}_C)(\nabla\cdot\overline{\mathbf{v}_C})+ \right.$$
$$\left.+j\omega\boldsymbol{\sigma}'\mathbf{A}_C\cdot\overline{\mathbf{v}_C}+j\omega\boldsymbol{\sigma}'\nabla\phi_C\cdot\overline{\mathbf{v}_C}\right)d\Omega_C+$$
$$-\int_\Gamma\left(\frac{1}{\mu_C}(\nabla\times\mathbf{A}_C)\times\mathbf{n}_C\right)\cdot\overline{\mathbf{v}_C}d\Gamma-\frac{1}{\mu_*}\int_\Gamma(\overline{\mathbf{v}_C}\cdot\mathbf{n}_C)\nabla\cdot\mathbf{A}_C d\Gamma=\int_{\Omega_C}\mathbf{J}_{e,C}\cdot\overline{\mathbf{v}_C}d\Omega_C, \quad (26)$$

for Ω_C, and

$$\int_{\Omega_I}\left(\frac{1}{\mu_I}(\nabla\times\mathbf{A}_I)\cdot(\nabla\times\overline{\mathbf{v}_I})+\frac{1}{\mu_*}(\nabla\times\mathbf{A}_I)(\nabla\cdot\overline{\mathbf{v}_I})\right)d\Omega_I+$$
$$-\int_\Gamma\left(\frac{1}{\mu_I}(\nabla\times\mathbf{A}_I)\times\mathbf{n}_I\right)\cdot\overline{\mathbf{v}_I}d\Gamma-\frac{1}{\mu_*}\int_\Gamma(\overline{\mathbf{v}_I}\cdot\mathbf{n}_I)\nabla\cdot\mathbf{A}_I d\Gamma=\int_{\Omega_I}\mathbf{J}_{e,I}\cdot\overline{\mathbf{v}_I}d\Omega_I, \quad (27)$$

for Ω_I. Obviously, to achieve both (26) and (27), the seventh and eighth equations in (23) are exploited.

Since on Γ, both $\mathbf{n}_C\times(\mathbf{v}_C\times\mathbf{n}_C)=\mathbf{n}_I\times(\mathbf{v}_I\times\mathbf{n}_I)$ and $\mathbf{v}_C\cdot\mathbf{n}_C+\mathbf{v}_I\cdot\mathbf{n}_I=0$ hold, by summing these equations and considering the interface conditions (specifically the second and twelfth equations in (16)), we easily obtain

$$\int_{\Omega_C}\left(\frac{1}{\mu_C}(\nabla\times\mathbf{A}_C)\cdot(\nabla\times\overline{\mathbf{v}_C})+\frac{1}{\mu_*}(\nabla\cdot\mathbf{A}_C)(\nabla\cdot\overline{\mathbf{v}_C})\right)d\Omega_C+$$
$$+\int_{\Omega_C}(j\omega\boldsymbol{\sigma}'\mathbf{A}_C\cdot\overline{\mathbf{v}_C}+j\omega\boldsymbol{\sigma}'\nabla\phi_C\cdot\overline{\mathbf{v}_C})d\Omega_C+$$
$$+\int_{\Omega_I}\left(\frac{1}{\mu_I}(\nabla\times\mathbf{A}_I)\cdot(\nabla\times\overline{\mathbf{v}_I})+\frac{1}{\mu_*}(\nabla\cdot\mathbf{A}_I)(\nabla\cdot\overline{\mathbf{v}_I})\right)d\Omega_I=$$
$$=\int_{\Omega_C}\mathbf{J}_{e,C}\cdot\overline{\mathbf{v}_C}d\Omega_C+\int_{\Omega_I}\mathbf{J}_{e,I}\cdot\overline{\mathbf{v}_I}d\Omega_I. \quad (28)$$

Now, we multiply the third equation by the complex conjugate of ϕ_C, $\overline{\phi_C}$ and integrate over Ω_C.

Remark 8. *In CFRPs, the multiplication of the differential equation by* $\overline{\phi_C}$ *and the integration over* Ω_C *guarantee that the approximate solution is numerically stable, since it allows us to deal with functions that may not be perfectly smooth or that may present local discontinuities due to defects in the material. In other words, this procedure allows the effects due to defects to be integrated without requiring the solutions to be extremely smooth everywhere, which would be unrealistic in the presence of defects. Finally, this approach allows transferring some derivatives from the unknown function to the test functions, which are chosen to satisfy certain regularity properties, allowing to obtain stable and convergent approximate solutions.*

Furthermore, by performing integration by parts and making use of the fourth equation in (16), it is easy to achieve [33]

$$\int_{\Omega_C} (j\omega\boldsymbol{\sigma}'\mathbf{A}_C \cdot \nabla\overline{\phi_C} + j\omega\boldsymbol{\sigma}'\nabla\phi_C \cdot \nabla\overline{\phi_C})d\Omega_C = \int_{\Omega_C} \mathbf{J}_{e,C} \cdot \nabla\overline{\phi_C}d\Omega_C + \int_{\Gamma} \mathbf{J}_{e,I} \cdot \mathbf{n}_I\overline{\phi_C}d\Gamma. \quad (29)$$

When we multiply the third equation by the complex conjugate of ϕ_C, $\overline{\phi_C}$, and integrate over Ω_C, we obtain an expression that represents the integration of the electrical components as a function of the scalar potentials and vector. This step is essential to constructing an energy functional which includes all energy contributions relevant in the Ω domain.

Therefore, to encapsulate the physical properties and constraints of the system, the energy functional, $\mathcal{E}[(\mathbf{A}_C, \phi_C), (\mathbf{v}, \Phi_C)]$, designed to include all relevant energy contributions in Ω, represents the integral of the contributions of the magnetic energy, the electrical energy and the terms of coupling between the magnetic vector potential and the electric scalar potential. In particular [33],

$$\begin{aligned}\mathcal{E}[(\mathbf{A}_C, \phi_C), (\mathbf{v}, \Phi_C))] := \int_{\Omega} \left(\frac{1}{\mu}(\nabla \times \mathbf{A}) \cdot (\nabla \times \overline{\mathbf{v}}) + \frac{1}{\mu_*}(\nabla \cdot \mathbf{A})(\nabla \cdot \overline{\mathbf{v}})\right) d\Omega + \\ + \int_{\Omega_C} (j\omega\boldsymbol{\sigma}'\mathbf{A}_C \cdot \overline{\mathbf{v}_C} + j\omega\boldsymbol{\sigma}'\nabla\phi_C \cdot \overline{\mathbf{v}_C})d\Omega_C + \\ + \int_{\Omega_C} (j\omega\boldsymbol{\sigma}'\mathbf{A}_C \cdot \nabla\overline{\Phi_C} + j\omega\boldsymbol{\sigma}'\nabla\phi_C \cdot \nabla\overline{\Phi_C})d\Omega_C. \quad (30)\end{aligned}$$

Remark 9. *The energy functional $\mathcal{E}$ is defined over the entire domain Ω, which includes both Ω_C (the CFRP plate) and the insulating domain Ω_I. However, in this work, we refer to $\mathcal{E}[(\mathbf{A}_C, \phi_C), (\mathbf{v}, \Phi_C)]$, where $\mathbf{A}_C$ and ϕ_C represent the vector potential and scalar potential in the conductive domain Ω_C, respectively. This choice is justified by the fact that the problem primarily focuses on Ω_C, as it is within this domain that the main electromagnetic interactions relevant to defect characterization occur. Although the energy functional depends on the electromagnetic behavior across the entire domain Ω, the behavior in the insulating domain Ω_I plays an auxiliary role, mainly serving to satisfy boundary conditions and ensure solution continuity. Consequently, the primary focus is on $\mathbf{A}_C$ and ϕ_C in Ω_C, where the most critical analysis takes place. Additionally, the interface conditions between Ω_C and Ω_I allow the contribution of the insulating domain Ω_I to be expressed in terms of the quantities defined on Ω_C. This justifies the decision to focus on $\mathbf{A}_C$ and ϕ_C in the variational formulation and numerical calculations, as these quantities are sufficient to accurately describe the system in the conductive domain while also indirectly addressing the insulating domain. Finally, this choice simplifies the computational problem by avoiding the need to explicitly solve the equations over the entire domain Ω. By focusing the analysis on $\mathbf{A}_C$ and ϕ_C, computational efficiency is improved, as attention is directed to variables that directly impact the relevant electromagnetic properties of the material.*

Each term of (30) represents specific components of electromagnetic energy and the interactions between $\mathbf{A}$ and ϕ. Let us look at each term in detail as it relates to CFRP plates. The term $\int_{\Omega} \frac{1}{\mu}(\nabla \times \mathbf{A}) \cdot (\nabla \times \overline{\mathbf{v}})d\Omega$ represents the magnetic energy stored in the system (probe-plate) where $\nabla \times \mathbf{A}$ is related to $\mathbf{H}$. μ^{-1} considers the magnetic permeability of the CFRP material, locally variable in Ω, which could present inhomogeneities due to the presence of carbon fibers and the polymer matrix. It follows that any variation in permeability could significantly influence the distribution of $\mathbf{H}$ (and therefore of $\mathbf{B}$) within the composite material.

The term $\int_{\Omega} \frac{1}{\mu_*}(\nabla \cdot \mathbf{A})(\nabla \cdot \overline{\mathbf{v}})d\Omega$ introducing the mediation constant of the magnetic permeability in Ω, μ_* guarantees the stabilization of the numerical solution which otherwise would not be ensured due to the variable anisotropic properties of the CFRP.

The term $\int_{\Omega_C}(j\omega\boldsymbol{\sigma}'\mathbf{A}_C\cdot\overline{\mathbf{v}_C}+j\omega\boldsymbol{\sigma}'\nabla\phi_C\cdot\overline{\mathbf{v}_C})d\Omega_C$ represents the electric energy and the coupling between $\mathbf{A}_C$ and ϕ_C within the domain Ω_C. Parameter $j\omega$ indicates that we are considering the steady-state sinusoidal regime, which is typical in electromagnetic analyses at constant frequency. The term $\boldsymbol{\sigma}'$ reflects the electrical conductivity of the CFRP material, considering any defects present. This term is crucial for representing ohmic losses and electrical energy dissipation in the material, as the electrical properties in CFRP composites can vary significantly due to discontinuities introduced by defects such as delamination, microcracks, and fiber breakages.

The term $\int_{\Omega_C}(j\omega\boldsymbol{\sigma}'\mathbf{A}_C\cdot\nabla\overline{\Phi_C}+j\omega\boldsymbol{\sigma}'\nabla\phi_C\cdot\nabla\overline{\Phi_C})d\Omega_C$ in (30) is essential for accurately modeling the electrical behavior of CFRP plates in a sinusoidal steady-state regime with defects. The first component, $j\omega\boldsymbol{\sigma}'\mathbf{A}_C\cdot\nabla\overline{\Phi_C}$, represents the interaction between $\mathbf{A}_C$ and ϕ_C for capturing the coupling effects between the magnetic and electric fields in the CFRP plate. The second component, $j\omega\boldsymbol{\sigma}'\nabla\phi_C\cdot\nabla\overline{\Phi_C}$, accounts for the ohmic losses and the dissipation of electrical energy within the material. This term ensures that (30) accurately reflects the electrical energy dissipation and provides a comprehensive description of the electromagnetic behavior of the CFRP plate.

Therefore, as in [33], problem (16) is equivalent to finding $(\mathbf{A},\phi_C)\in W\times H^1_2(\Omega_C)$ such that $\forall(\mathbf{v},\Phi_C)\in W\times H^1_{\#}(\Omega_C)$,

$$\mathcal{E}[(\mathbf{A}_C,\phi_C),(\mathbf{v},\Phi_C))]=\int_\Omega\mathbf{J}_e\cdot\overline{\mathbf{v}}d\Omega+\int_{\Omega_C}\mathbf{J}_{e,C}\cdot\nabla\overline{\Phi_C}d\Omega_C+\int_\Gamma\mathbf{J}_{e,I}\cdot\mathbf{n}_I\overline{\Phi_C}d\Gamma, \quad (31)$$

where

$$W:=\{\mathbf{v}\in H(\mathrm{curl};\Omega)\cap H(\mathrm{div};\Omega)\mid\mathbf{v}\cdot\mathbf{n}=0\text{ on }\partial\Omega,\ \ \mathcal{G}_k(\mathbf{v})=0,\ \ \forall k=1,\ldots,n_{\partial\Omega}\}, \quad (32)$$

and

$$H^1_{\#}(\Omega_C):=\{\Phi_C\in H^1(\Omega_C)\ \Big|\ \int_{\Omega_{C,i}}\Phi_{|\Omega_{C,i}}d\Omega_{C,i}=0\ \ \forall i=1,\ldots,p_\Gamma\}. \quad (33)$$

Remark 10. *The use of complex test functions rather than real ones is necessary because the fields considered operate in a permanent sinusoidal regime, often involving a complex exponential. Therefore, it is essential to formulate the problem in the Fourier domain. When formulating the weak problem, it is necessary to consider scalar products defined to incorporate the oscillating properties of the fields involved. Integrating these scalar products maintains the orthogonality and energy conservation properties, accounting for the phase and amplitude components of each field. Additionally, complex test functions offer significant analytical advantages due to their stronger differentiability properties compared to real functions.*

Remark 11. (33) *proposed in [33] is suitable for several reasons related to the mathematical and physical properties of the solutions of our electromagnetic problem with CFRP plates not presenting significant topological complexities such as holes or cavities (obviously, the analyzed CFRP plates do not present rivets and/or bolts or holes/cavities of other nature, where the NdT techniques used are purely specific). This makes using $H^1(\Omega_C)$ appropriate to describe the properties of* $\mathbf{E}$ *in* Ω_C *within the domain because it includes quadratically integrable functions on* Ω_C *together with its defined first derivatives (sufficiently smooth solutions). The addition of condition* $\int_{\Omega_{C,i}}\Phi_{|\Omega_{C,i}}=0\ \ \forall i=1,\ldots,p_\Gamma$ *implies that the mean of* Φ_C*, on each connected component,* $\Omega_{C,i}$*, is zero to ensure the uniqueness of the solution to the problem defined up to an additive constant (the zero mean eliminates this indeterminacy, making the problem well posed).*

9. Existence and Uniqueness of the Solution to the Weak Formulation

The CFRP plates used in the benchmark feature relatively simple geometry, without holes or significant topological complexity. This implies that the domain can be considered simply connected, where every closed cycle can be contracted to a point without leaving the domain; there are no cycles of the second type (i.e., cycles that do not delimit a surface contained in the domain itself). Moreover, since the domain is simply connected, we can

assume that there are no cycles of the second type. This means we do not need additional conditions to handle these loops, which translates to $n_{\partial\Omega} = 0$.

Condition $n^*_{\partial\Omega} = 0$ comes from the fact that Ω does not require additional conditions to obtain a global potential. This happens when there are no non-bounded loops intersecting Ω_C. In our case, the considered CFRP plates do not exhibit such cycles due to its simple and regular structure. Since there are no complex cycles requiring further conditions, we can obtain the existence and uniqueness of the global potential without needing to consider more complex cases. This greatly simplifies our analysis and allows us to focus exclusively on the case of $n_{\partial\Omega} = n^*_{\partial\Omega} = 0$.

Therefore, starting from [33], the existence and uniqueness result can be achieved exploiting (a) the Lax–Milgram Lemma [40]; (b) the trace theorems from $H(\mathrm{div};\Omega_I)$ onto $H^{-1/2}(\Gamma)$ and from $H^1(\Omega_C)$ onto $H^{1/2}(\Gamma)$ (for the statements of these theorems, see Appendix A); (c) Cauchy–Schwarz inequality; the Poincaré inequality.

The following result concerning the existence and uniqueness of the solution to the weak formulation holds [33].

Theorem 4 (Existence and Uniqueness)**.** *The weak formulation of the problem under study admits only one solution.*

Proof of Theorem 4. In retracing all the steps of the result already discussed in [33], we highlight useful engineering clarifications.

Since $(W \times H^1_{\#}(\Omega_C))$ is clearly a Hilbert space with respect to the natural scalar product, and the sesquilinear form $\mathcal{E}[\cdot,\cdot]$ is continuous in $(W \times H^1_{\#}(\Omega_C)) \times (W \times H^1_{\#}(\Omega_C))$, we only need to verify that the right-hand side in (32) and (33) is a continuous (antilinear) functional in $W \times H^1_{\#}(\Omega_C)$ and that $\mathcal{E}[\cdot,\cdot]$ is coercive in $(W \times H^1_{\#}(\Omega_C)) \times (W \times H^1_{\#}(\Omega_C))$. Specifically, there must exist a constant $k_0 > 0$ such that for every $(\mathbf{v}, \Phi_C) \in W \times H^1_{\#}(\Omega_C)$,

$$\Big|\mathcal{E}[(\mathbf{v},\Phi_C),(\mathbf{v},\Phi_C)]\Big| \geq$$
$$\geq k_0\left(\int_\Omega (|\mathbf{v}|^2 + |\nabla\times\mathbf{v}|^2 + |\nabla\cdot\mathbf{v}|^2)d\Omega + \int_{\Omega_C}(|\Phi_C|^2 + |\nabla\Phi_C|^2)d\Omega_C\right). \tag{34}$$

In EC testing, coercivity in the mathematical model ensures that measured responses are proportional and consistent with the presence of defects that are identified without false positives or negatives. Furthermore, the higher the coercivity, the greater the ability of the test to detect small changes in the behavior of the magnetic field caused by even small defects. Furthermore, EC-based tests that take advantage of coercivity can be performed quickly, reducing time and costs. Finally, coercivity supports the development of standardized and repeatable testing protocols.

On the right hand of (32) and (33), the only term to check is the third one. We have

$$\left|\int_\Gamma (\mathbf{J}_{e,I}\cdot\mathbf{n}_I)\overline{\Phi_C}d\Gamma\right| \leq C_1\|\mathbf{J}_{e,I}\cdot\mathbf{n}_I\|_{H^{-1/2}(\Gamma)}\|\Phi_C\|_{H^{1/2}(\Gamma)} \leq C_2\|\mathbf{J}_{e,I}\|_{L^2(\Omega_I)}\|\Phi_C\|_{H^1(\Omega_C)}, \tag{35}$$

having used the trace theorem from $H(\mathrm{div};\Omega_I)$ onto $H^{-1/2}(\Gamma)$ and from $H^1(\Omega_C)$ onto $H^{1/2}(\Gamma)$ (for the statement of this theorem, see Appendix A).

The passage focuses on the term $\int_\Gamma (\mathbf{J}_{e,I}\cdot\mathbf{n}_I)\overline{\phi_C}d\Gamma$ of the equation which represents the integral over the surface Γ of the dot product between $\mathbf{J}_{e,I}$ and $\mathbf{n}_I$, multiplied by the complex conjugate of the potential ϕ_C. Practically, this term is critical, as it links the boundary conditions of the external electric field with the physical properties of the CFRP material. Moreover, the inequality used estimates the magnitude of this term through functional norms. The norm $\|\mathbf{J}_{e,I}\cdot\mathbf{n}_I\|_{H^{-1/2}(\Gamma)}$ measures the magnitude of the component of the external current density normal to the surface Γ in a generalized sense (Sobolev space), which is relevant to understand how effectively the external current interacts with the material surface. Finally, the passage highlights the application of the trace theorem,

which allows linking norms defined on larger domains (like $L^2(\Omega_I)$ and $H^1(\Omega_C)$) with norms defined on contours or surfaces (like $H^{-1/2}(\Gamma)$). This is fundamental in materials engineering, especially in CFRPs, where boundary properties can significantly influence the material's response to external stimuli such as induced currents.

Regarding inequality (34), it is easy to write

$$\mathcal{E}[(\mathbf{v},\Phi_C),(\mathbf{v},\Phi_C))] = \int_\Omega \left(\frac{1}{\mu}(\nabla\times\mathbf{v})\cdot(\nabla\times\overline{\mathbf{v}}) + \frac{1}{\mu_*}|\nabla\cdot\mathbf{v}|^2\right)d\Omega + \\ + j\omega\int_{\Omega_C}(\boldsymbol{\sigma}'\mathbf{v}_C\cdot\overline{\mathbf{v}_C} + \boldsymbol{\sigma}'\nabla\Phi_C\cdot\nabla\overline{\Phi_C} + \boldsymbol{\sigma}'\nabla\Phi_C\cdot\overline{\mathbf{v}_C} + \boldsymbol{\sigma}'\mathbf{v}_C\cdot\nabla\overline{\Phi_C})d\Omega_C, \tag{36}$$

from which, since $\boldsymbol{\sigma}'\nabla\Phi_C\cdot\overline{\mathbf{v}_C} + \boldsymbol{\sigma}'\mathbf{v}_C\cdot\nabla\overline{\Phi_C} = 2\mathrm{Re}(\boldsymbol{\sigma}'\nabla\Phi_C\cdot\overline{\mathbf{v}_C})$ (see Appendix B), we obtain

$$\left|\mathcal{E}[(\mathbf{v},\Phi_C),(\mathbf{v},\Phi_C))]\right|^2 = \left(\int_\Omega \left(\frac{1}{\mu}(\nabla\times\mathbf{v})\cdot(\nabla\times\overline{\mathbf{v}}) + \frac{1}{\mu_*}|\nabla\cdot\mathbf{v}|^2\right)d\Omega\right)^2 + \\ + \omega^2\left(\int_{\Omega_C}(\boldsymbol{\sigma}'\mathbf{v}_C\cdot\overline{\mathbf{v}_C} + \boldsymbol{\sigma}'\nabla\Phi_C\cdot\nabla\overline{\Phi_C} + 2\mathrm{Re}(\boldsymbol{\sigma}'\nabla\Phi_C\cdot\overline{\mathbf{v}_C}))d\Omega_C\right)^2. \tag{37}$$

On the other hand, given a couple of real numbers a e b, being $(a+b)^2 \geq \frac{1}{2}a^2 - b^2$ and also $(a+b)^2 \geq 2\rho(a+b)^2 \geq \rho a^2 - 2\rho b^2$ for each $0 < \rho \leq \frac{1}{2}$ (besides the fact that $|ab| \leq \frac{1}{16}a^2 + 4b^2$), inequality (36), applying the Cauchy–Schwarz inequality, becomes

$$\omega^2\left(\int_{\Omega_C}(\boldsymbol{\sigma}'\mathbf{v}_C\cdot\overline{\mathbf{v}_C}\cdot + \boldsymbol{\sigma}'\nabla\Phi_C\cdot\nabla\overline{\Phi_C} + 2\mathrm{Re}(\boldsymbol{\sigma}'\nabla\Phi_C\cdot\overline{\mathbf{v}_C}))d\Omega_C\right)^2 \geq \\ \geq \frac{\omega^2\rho}{2}\sigma^2_{\min}\left(\int_{\Omega_C}|\nabla\Phi_C|^2 d\Omega_C\right)^2 - 31\omega^2\rho\sigma^2_{\max}\left(\int_{\Omega_C}|\mathbf{v}_C|^2 d\Omega_C\right)^2, \tag{38}$$

where $\sigma^2_{\max}$ and $\sigma^2_{\min}$ are the maximum and minimum eigenvalues of $\boldsymbol{\sigma}'$ in Ω_C, respectively. The Cauchy–Schwarz inequality and the estimate $|ab| \leq \frac{1}{16}a^2 + 4b^2$ are exploited.

It is worth noting that the use of $\sigma^2_{\max}$ and $\sigma^2_{\min}$ contributes to the stability and distribution of ECs within the CFRP by defining the extreme limits of the electrical properties of the material (usually along preferred directions). In particular, knowing the eigenvalues allows us to predict areas of potential heat accumulation due to ECs, which can cause thermal or mechanical damage if not managed adequately. These phenomena can compromise the safety and reliability of CFRP components.

Furthermore, using the Poincaré inequality, one can also conclude that there exists a constant $K_1 > 0$ such that

$$\int_{\Omega_C}|\nabla\Phi_C|^2 d\Omega_C = \sum_{i=1}^{p_\Gamma}\int_{\Omega_{C,i}}|\nabla\Phi_{C|\Omega_{C,i}}|^2 d\Omega_{C,i} \geq K_1\int_{\Omega_C}(|\nabla\Phi_C|^2 + |\Phi_C|^2)d\Omega_C. \tag{39}$$

The equation used for EC in CFRP materials is interpreted as an inequality (see (39)) within Ω_C. This inequality establishes that the integral of the energy of the gradient of the electric potential Φ_C across the entire domain Ω exceeds the sum of the integrals of the energies of the gradient and the potential itself over specific subdomains, multiplied by a constant. Equation (39) reflects a fundamental property of Φ_C, linking spatial variations of the potential to its magnitudes across various material regions (since Ω_C is divided into different regions $\Omega_{C,i}$), each potentially corresponding to areas of the material with different

electrical characteristics, such as variations caused by defects or discontinuities in the fiber or matrix. The inequality indicates that the total electric field energy in the material cannot be less than the sum of the energies measured locally, adjusted by a constant dependent on the material's physical properties. Practically, this inequality is essential for non-destructive tests based on EC, as it provides a robust mathematical basis that ensures the predictability and reliability of the material's response to induced currents. It is particularly useful to ensure that minimal variations in potential, caused by defects, are detectable. The inequality ensures that local fluctuations in the electric field are significant enough to be detected through standardized testing methods. The interpretation and application of this inequality in the design and analysis of CFRP materials are crucial for the development of advanced engineering solutions, particularly in sectors such as aerospace and automotive, where safety and performance requirements are extremely stringent. This confirms that the models used to simulate the behavior of materials under electrical stress are robust and reliable, thus enhancing the effectiveness of non-destructive testing and significantly contributing to the safety and reliability of critical components used in various industrial applications.

Moreover, since $n_{\partial\Omega} = n^*_{\partial\Omega} = 0$, there exists a constant $K_2 > 0$ such that for any function $\mathbf{v} \in W$, one has

$$\left(\int_\Omega \frac{1}{\mu}((\nabla \times \mathbf{v}) \cdot (\nabla \times \overline{\mathbf{v}}) + \frac{1}{\mu_*}|\nabla \cdot \mathbf{v}|^2) d\Omega \right)^2 \geq$$
$$\geq K_2^2 \left(\int_\Omega (|\nabla \times \mathbf{v}|^2 + |\nabla \cdot \mathbf{v}|^2 + |\mathbf{v}|^2) d\Omega \right)^2, \tag{40}$$

where $\mu_{\max}$ is the maximum eigenvalue for μ in Ω. Moreover, choosing ρ such that $31\omega^2 \boldsymbol{\sigma}'_{\max} \rho < K_2^2$ and $0 < \rho < \frac{1}{2}$, from (36)–(40), we find at once (34).

The examined inequality correlates the magnetic field and induced currents with material properties via rotational and divergent gradients. The magnetic permeability eigenvalues, $\mu_{\max}$ and μ_* capture the limits of the magnetic properties within the Ω domain, essential for controlling the total energy of the system and ensuring energy stability. The constant K_2 and the choice of ρ guarantee that energy fluctuations remain confined within safe limits, thus preventing unwanted effects such as overheating.

Particularly, (34) was claimed by the authors of [33] who considered the Coulomb gauged and the Lorentz gauged vector potential formulations of the EC problem, respectively; however, this proof does not seem to be complete, and it is valid only for small value of ω. Indeed, for completing the proof, it seems necessary to consider the crucial estimate (40). □

10. Some Food for Thought on Stability

The fact that the energy functional is coercive guarantees the stability of the numerical approach for the approximate solution. However, in the energy functional, the term involving $\nabla \cdot \mathbf{v}$ has less impact than the terms involving $\nabla \times \mathbf{v}$ (the magnetic energy and associated fields are described mainly in terms of rotor). So, we ask ourselves whether stability is still assured, even in this case. To analyze the stability of the solution in terms of perturbation of the conductivity tensor due to defects, we consider a perturbation of the conductivity tensor $\boldsymbol{\sigma}'$ in the Ω_C domain, which becomes $\boldsymbol{\sigma}' + \delta\boldsymbol{\sigma}'$, where $\delta\boldsymbol{\sigma}'$ represents the change in the conductivity tensor due to perturbation. Therefore, in unperturbed conditions, we have

$$\mathcal{E}_1[(\mathbf{A}_C, \phi_C), (\mathbf{v}, \Phi_C)] = \int_\Omega \frac{1}{\mu}(\nabla \times \mathbf{A}) \cdot (\nabla \times \overline{\mathbf{v}}) d\Omega + \int_{\Omega_C} j\omega \boldsymbol{\sigma}' \mathbf{A}_C \cdot \overline{\mathbf{v}_C} d\Omega_C +$$
$$+ \int_{\Omega_C} j\omega \boldsymbol{\sigma}' \nabla\phi_C \cdot \overline{\mathbf{v}_C} d\Omega_C + \int_{\Omega_C} j\omega \boldsymbol{\sigma}' \mathbf{A}_C \cdot \nabla\overline{\Phi_C} d\Omega_C + \int_{\Omega_C} j\omega \boldsymbol{\sigma}' \nabla\phi_C \cdot \nabla\overline{\Phi_C} d\Omega_C. \tag{41}$$

In the perturbed case, the energy functional is defined as

$$\mathcal{E}_1^{\text{pert}}[(\mathbf{A}_C^{\text{pert}}, \phi_C^{\text{pert}}), (\mathbf{v}, \Phi_C)] = \int_\Omega \frac{1}{\mu}(\nabla \times \mathbf{A}) \cdot (\nabla \times \overline{\mathbf{v}}) d\Omega + \\ + \int_{\Omega_C} j\omega(\boldsymbol{\sigma}' + \delta\boldsymbol{\sigma}')\mathbf{A}_C^{\text{pert}} \cdot \overline{\mathbf{v}_C} d\Omega_C + \int_{\Omega_C} j\omega(\boldsymbol{\sigma}' + \delta\boldsymbol{\sigma}')\nabla\phi_C^{\text{pert}} \cdot \overline{\mathbf{v}_C} d\Omega_C + \\ + \int_{\Omega_C} j\omega(\boldsymbol{\sigma}' + \delta\boldsymbol{\sigma}')\mathbf{A}_C^{\text{pert}} \cdot \nabla\overline{\Phi_C} d\Omega_C + \int_{\Omega_C} j\omega(\boldsymbol{\sigma}' + \delta\boldsymbol{\sigma}')\nabla\phi_C^{\text{pert}} \cdot \nabla\overline{\Phi_C} d\Omega_C \tag{42}$$

Remark 12. *The choice to make $\Delta\mathcal{E}_1$ depend solely on $\mathbf{A}_C$ is intentional. In particular, while the complete functional $\mathcal{E}_1$ depends on $\mathbf{A}$ over all Ω (see Remark 9), the perturbed functional $\Delta\mathcal{E}_1$ was constructed to focus on defect-induced local variations within Ω_C. This approach simplifies the perturbation analysis, since $\mathbf{A}_C$ is the component of $\mathbf{A}$ that directly contributes to the electromagnetic variations relevant for defect detection and characterization. The choice to consider only $\mathbf{A}_C$ in the definition of $\Delta\mathcal{E}_1$ also reflects the need to reduce computational complexity while maintaining modeling accuracy in the regions of main interest.*

Remark 13. *The analysis carried out in the paper focuses mainly on $\mathcal{E}_1$ to simplify the treatment of the problem and to highlight the local variations induced by defects in Ω_C. However, if we consider the full energy functional $\mathcal{E}$, the analysis remains conceptually consistent, but with some operational differences. In particular, the inclusion of the functional integer $\mathcal{E}$ implies an explicit treatment of electromagnetic interactions in both Ω_C and Ω_I. This would lead to greater computational complexity, since it would be necessary to consider the field influences on the whole Ω, including those of the insulating domain Ω_I, which in some cases can have a marginal impact on the detection of defects in the CFRP plate. From a theoretical perspective, the transition from the analysis of $\mathcal{E}_1$ to $\mathcal{E}$ does not alter the fundamental conclusions of the work but requires a more complex management of the boundary conditions and numerical solutions, with a consequent increase in computational cost. The choice to focus on $\mathcal{E}_1$ is therefore motivated by the desire to obtain an effective and precise solution in the regions of greatest physical interest, minimizing complications that do not make significant contributions to the defect analysis.*

The difference between the two functionals is given by

$$\Delta\mathcal{E}_1 = \mathcal{E}_1^{\text{pert}}[(\mathbf{A}_C^{\text{pert}}, \phi_C^{\text{pert}}), (\mathbf{v}, \Phi_C)] - \mathcal{E}_1[(\mathbf{A}_C, \phi_C), (\mathbf{v}, \Phi_C)] = \\ = \Bigg(\int_{\Omega_C} j\omega(\boldsymbol{\sigma}' + \delta\boldsymbol{\sigma}')\mathbf{A}_C^{\text{pert}} \cdot \overline{\mathbf{v}_C} d\Omega_C + \\ + \int_{\Omega_C} j\omega(\boldsymbol{\sigma}' + \delta\boldsymbol{\sigma}')\nabla\phi_C^{\text{pert}} \cdot \overline{\mathbf{v}_C} d\Omega_C + \int_{\Omega_C} j\omega(\boldsymbol{\sigma}' + \delta\boldsymbol{\sigma}')\mathbf{A}_C^{\text{pert}} \cdot \nabla\overline{\Phi_C} d\Omega_C + \\ + \int_{\Omega_C} j\omega(\boldsymbol{\sigma}' + \delta\boldsymbol{\sigma}')\nabla\phi_C^{\text{pert}} \cdot \nabla\overline{\Phi_C} d\Omega_C \Bigg) - \Bigg(\int_{\Omega_C} j\omega\boldsymbol{\sigma}'\mathbf{A}_C \cdot \overline{\mathbf{v}_C} d\Omega_C + \\ + \int_{\Omega_C} j\omega\boldsymbol{\sigma}'\nabla\phi_C \cdot \overline{\mathbf{v}_C} d\Omega_C + \int_{\Omega_C} j\omega\boldsymbol{\sigma}'\mathbf{A}_C \cdot \nabla\overline{\Phi_C} d\Omega_C + \int_{\Omega_C} j\omega\boldsymbol{\sigma}'\nabla\phi_C \cdot \nabla\overline{\Phi_C} d\Omega_C \Bigg). \tag{43}$$

Remark 14. *Let us consider two solutions: the original one $(\mathbf{A}_C, \phi_C)$ and the perturbed one $(\mathbf{A}_C^{pert}, \phi_C^{pert})$. To find a relation that allows us to analyze $\delta\mathbf{A}_C$ and $\delta\phi_C$, we subtract the equation of the original bilinear functional, $\mathcal{E}_1[(\mathbf{A}_C, \phi_C), (\mathbf{v}, \Phi_C)] = F[(\mathbf{v}, \Phi_C)]$, from the perturbed one, $\mathcal{E}_1^{pert}[(\mathbf{A}_C^{pert}, \phi_C^{pert}), (\mathbf{v}, \Phi_C)] = F^{pert}[(\mathbf{v}, \Phi_C)]$, where $F[(\mathbf{v}, \Phi_C)]$ and $F^{pert}[(\mathbf{v}, \Phi_C)]$ are the functionals corresponding to the original and perturbed problems, respectively. In eddy current problems, $F[(\mathbf{v}, \Phi_C)]$ represents the part of the problem that does not directly depend on the material properties but rather on the external current sources and applied fields. Introducing a perturbation in the conductivity tensor modifies only part of the equations that describe the electromagnetic field behavior inside the material. However, the external current sources are not altered by the presence of*

defects in the material. Therefore, the linear functional, which depends on these external sources, remains unchanged, $F^{pert}[(\mathbf{v}, \Phi_C)] = F[(\mathbf{v}, \Phi_C)]$ (in other words, this condition allows writing $\Delta\mathcal{E} = 0$).

Remembering that $\mathbf{A}_C^{\text{pert}} = \mathbf{A}_C + \delta\mathbf{A}_C$ and $\phi_C^{\text{pert}} = \phi_C + \delta\phi_C$ and neglecting the second-order terms, the first integral in (43) becomes

$$\int_{\Omega_C} j\omega(\boldsymbol{\sigma}' + \delta\boldsymbol{\sigma}')\mathbf{A}_C^{\text{pert}} \cdot \overline{\mathbf{v}_C} d\Omega_C = \int_{\Omega_C} j\omega(\boldsymbol{\sigma}' + \delta\boldsymbol{\sigma}')(\mathbf{A}_C + \delta\mathbf{A}_C) \cdot \overline{\mathbf{v}_C} d\Omega_C = \\ = \int_{\Omega_C} j\omega(\boldsymbol{\sigma}'\mathbf{A}_C + \boldsymbol{\sigma}'\delta\mathbf{A}_C + \delta\boldsymbol{\sigma}'\mathbf{A}_C) \cdot \overline{\mathbf{v}_C} d\Omega_C, \quad (44)$$

while the second integral becomes

$$\int_{\Omega_C} j\omega(\boldsymbol{\sigma}' + \delta\boldsymbol{\sigma}')\nabla\phi_C^{\text{pert}} \cdot \overline{\mathbf{v}_C} d\Omega_C = \int_{\Omega_C} j\omega(\boldsymbol{\sigma}' + \delta\boldsymbol{\sigma}')\nabla(\phi_C + \delta\phi_C) \cdot \overline{\mathbf{v}_C} d\Omega_C = \\ = \int_{\Omega_C} j\omega(\boldsymbol{\sigma}' + \delta\boldsymbol{\sigma}')\nabla\phi_C \cdot \overline{\mathbf{v}_C} d\Omega_C + \int_{\Omega_C} j\omega(\boldsymbol{\sigma}' + \delta\boldsymbol{\sigma}')\nabla(\delta\phi_C) \cdot \overline{\mathbf{v}_C} d\Omega_C = \\ = \int_{\Omega_C} j\omega\boldsymbol{\sigma}'\nabla\phi_C \cdot \overline{\mathbf{v}_C} d\Omega_C + \int_{\Omega_C} j\omega\delta\boldsymbol{\sigma}'\nabla\phi_C \cdot \overline{\mathbf{v}_C} d\Omega_C + \\ + \int_{\Omega_C} j\omega\boldsymbol{\sigma}'\nabla(\delta\phi_C) \cdot \overline{\mathbf{v}_C} d\Omega_C + \int_{\Omega_C} j\omega\delta\boldsymbol{\sigma}'\nabla(\delta\phi_C) \cdot \overline{\mathbf{v}_C} d\Omega_C. \quad (45)$$

Likewise, the third integral can be developed as follows:

$$\int_{\Omega_C} j\omega(\boldsymbol{\sigma}' + \delta\boldsymbol{\sigma}')\mathbf{A}_C^{\text{pert}} \cdot \nabla\overline{\Phi_C} d\Omega_C = \int_{\Omega_C} j\omega(\boldsymbol{\sigma}' + \delta\boldsymbol{\sigma}')(\mathbf{A}_C + \delta\mathbf{A}_C) \cdot \nabla\overline{\Phi_C} d\Omega_C = \\ = \int_{\Omega_C} j\omega(\boldsymbol{\sigma}'\mathbf{A}_C + \boldsymbol{\sigma}'\delta\mathbf{A}_C + \delta\boldsymbol{\sigma}'\mathbf{A}_C) \cdot \nabla\overline{\Phi_C} d\Omega_C, \quad (46)$$

while the fourth integral provides

$$\int_{\Omega_C} j\omega(\boldsymbol{\sigma}' + \delta\boldsymbol{\sigma}')\nabla\phi_C^{\text{pert}} \cdot \nabla\overline{\Phi_C} d\Omega_C = \int_{\Omega_C} j\omega(\boldsymbol{\sigma}' + \delta\boldsymbol{\sigma}')\nabla(\phi_C + \delta\phi_C) \cdot \nabla\overline{\Phi_C} d\Omega_C = \\ = \int_{\Omega_C} j\omega(\boldsymbol{\sigma}' + \delta\boldsymbol{\sigma}')\nabla\phi_C \cdot \nabla\overline{\Phi_C} d\Omega_C + \int_{\Omega_C} j\omega(\boldsymbol{\sigma}' + \delta\boldsymbol{\sigma}')\nabla\delta\phi_C \cdot \nabla\overline{\Phi_C} d\Omega_C. \quad (47)$$

Then, substituting (44)–(47) in (43), we obtain

$$\Delta\mathcal{E}_1 = \int_{\Omega_C} j\omega(\boldsymbol{\sigma}'\delta\mathbf{A}_C + \delta\boldsymbol{\sigma}'\mathbf{A}_C) \cdot \overline{\mathbf{v}_C} d\Omega_C + \\ + \int_{\Omega_C} j\omega\delta\boldsymbol{\sigma}'\nabla\phi_C \cdot \overline{\mathbf{v}_C} d\Omega_C + \int_{\Omega_C} j\omega\boldsymbol{\sigma}'\nabla(\delta\phi_C) \cdot \overline{\mathbf{v}_C} d\Omega_C + \\ + \int_{\Omega_C} j\omega\delta\boldsymbol{\sigma}'\nabla(\delta\phi_C) \cdot \overline{\mathbf{v}_C} d\Omega_C + \int_{\Omega_C} j\omega(\boldsymbol{\sigma}'\delta\mathbf{A}_C + \delta\boldsymbol{\sigma}'\mathbf{A}_C) \cdot \nabla\overline{\Phi_C} d\Omega_C + \\ + \int_{\Omega_C} j\omega\delta\boldsymbol{\sigma}'\nabla\phi_C \cdot \nabla\overline{\Phi_C} d\Omega_C + \int_{\Omega_C} j\omega(\boldsymbol{\sigma}' + \delta\boldsymbol{\sigma}')\nabla(\delta\phi_C) \cdot \nabla\overline{\Phi_C} d\Omega_C, \quad (48)$$

from which, considering that $\Delta\mathcal{E}_1 = 0$, we can write

$$\begin{aligned}
&\int_{\Omega_C} j\omega\boldsymbol{\sigma}'\delta\mathbf{A}_C\cdot\overline{\mathbf{v}_C}d\Omega_C + \int_{\Omega_C} j\omega\boldsymbol{\sigma}'\nabla(\delta\phi_C)\cdot\overline{\mathbf{v}_C}d\Omega_C + \\
&+\int_{\Omega_C} j\omega\boldsymbol{\sigma}'\delta\mathbf{A}_C\cdot\nabla\overline{\Phi_C}d\Omega_C + \int_{\Omega_C} j\omega\boldsymbol{\sigma}'\nabla(\delta\phi_C)\cdot\nabla\overline{\Phi_C}d\Omega_C = \\
&= -\int_{\Omega_C} j\omega\delta\boldsymbol{\sigma}'\mathbf{A}_C\cdot\overline{\mathbf{v}_C}d\Omega_C - \int_{\Omega_C} j\omega\delta\boldsymbol{\sigma}'\nabla\phi_C\cdot\overline{\mathbf{v}_C}d\Omega_C - \\
&-\int_{\Omega_C} j\omega\delta\boldsymbol{\sigma}'\nabla(\delta\phi_C)\cdot\overline{\mathbf{v}_C}d\Omega_C - \int_{\Omega_C} j\omega\delta\boldsymbol{\sigma}'\mathbf{A}_C\cdot\nabla\overline{\Phi_C}d\Omega_C - \\
&-\int_{\Omega_C} j\omega\delta\boldsymbol{\sigma}'\nabla\phi_C\cdot\nabla\overline{\Phi_C}d\Omega_C - \int_{\Omega_C} j\omega\delta\boldsymbol{\sigma}'\nabla(\delta\phi_C)\cdot\nabla\overline{\Phi_C}d\Omega_C. \qquad (49)
\end{aligned}$$

Therefore, from (49) and applying the Cauchy–Schwarz inequality, we can write (remember that $\omega > 0$)

$$\begin{aligned}
&\left|\int_{\Omega_C} j\boldsymbol{\sigma}'\delta\mathbf{A}_C\cdot\overline{\mathbf{v}_C}d\Omega_C + \int_{\Omega_C} j\boldsymbol{\sigma}'\nabla(\delta\phi_C)\cdot\overline{\mathbf{v}_C}d\Omega_C + \right. \\
&\left. +\int_{\Omega_C} j\boldsymbol{\sigma}'\delta\mathbf{A}_C\cdot\nabla\overline{\Phi_C}d\Omega_C + \int_{\Omega_C} j\boldsymbol{\sigma}'\nabla(\delta\phi_C)\cdot\nabla\overline{\Phi_C}d\Omega_C\right| \leq \\
&\leq \int_{\Omega_C} |j\delta\boldsymbol{\sigma}'\mathbf{A}_C\cdot\overline{\mathbf{v}_C}|d\Omega_C + \int_{\Omega_C} |j\delta\boldsymbol{\sigma}'\nabla\phi_C\cdot\overline{\mathbf{v}_C}|d\Omega_C + \\
&+\int_{\Omega_C} |j\delta\boldsymbol{\sigma}'\nabla(\delta\phi_C)\cdot\overline{\mathbf{v}_C}|d\Omega_C + \int_{\Omega_C} |j\delta\boldsymbol{\sigma}'\mathbf{A}_C\cdot\nabla\overline{\Phi_C}|d\Omega_C + \\
&+\int_{\Omega_C} |j\delta\boldsymbol{\sigma}'\nabla\phi_C\cdot\nabla\overline{\Phi_C}|d\Omega_C + \int_{\Omega_C} |j\delta\boldsymbol{\sigma}'\nabla(\delta\phi_C)\cdot\nabla\overline{\Phi_C}|d\Omega_C = \\
&= \left[(\|\overline{\mathbf{v}_C}\|_{L^2(\Omega_C)} + \|\nabla\overline{\Phi_C}\|_{L^2(\Omega_C)})\|\mathbf{A}_C\|_{L^2(\Omega_C)} + \right. \\
&+(\|\overline{\mathbf{v}_C}\|_{L^2(\Omega_C)} + \|\nabla\overline{\Phi_C}\|_{L^2(\Omega_C)})\|\nabla\phi_C\|_{L^2(\Omega_C)} + \\
&\left.+(\|\overline{\mathbf{v}_C}\|_{L^2(\Omega_C)} + \|\nabla\overline{\Phi_C}\|_{L^2(\Omega_C)})\|\nabla(\delta\phi_C)\|_{L^2(\Omega_C)}\right]\|\delta\boldsymbol{\sigma}'\|_{L^2(\Omega_C)} = \\
&= \|\delta\boldsymbol{\sigma}'\|_{L^2(\Omega_C)}(\|\overline{\mathbf{v}_C}\|_{L^2(\Omega_C)} + \|\nabla\overline{\Phi_C}\|_{L^2(\Omega_C)})(\|\mathbf{A}_C\|_{L^2(\Omega_C)} + \\
&+\|\nabla\phi_C\|_{L^2(\Omega_C)} + \|\nabla(\delta\phi_C)\|_{L^2(\Omega_C)}) \qquad (50)
\end{aligned}$$

From inequality (50), it is easy to highlight that if $\|\delta\boldsymbol{\sigma}'\| \to 0$, it follows that

$$\begin{aligned}
&\left|\int_{\Omega_C} j\boldsymbol{\sigma}'\delta\mathbf{A}_C\cdot\overline{\mathbf{v}_C}d\Omega_C + \int_{\Omega_C} j\boldsymbol{\sigma}'\nabla(\delta\phi_C)\cdot\overline{\mathbf{v}_C}d\Omega_C + \right. \\
&\left. +\int_{\Omega_C} j\boldsymbol{\sigma}'\delta\mathbf{A}_C\cdot\nabla\overline{\Phi_C}d\Omega_C + \int_{\Omega_C} j\boldsymbol{\sigma}'\nabla(\delta\phi_C)\cdot\nabla\overline{\Phi_C}d\Omega_C\right| \to 0 \qquad (51)
\end{aligned}$$

Equation (51) represents a combination of integrals involving variations of the vector potential $\delta\mathbf{A}_C$, variations of the scalar potential $\delta\phi_C$, and their respective test functions $\overline{\mathbf{v}_C}$ and $\overline{\Phi_C}$. Physically, this expression describes how variations in the potentials affect the perturbed energy functional in the presence of perturbed conductivity $\boldsymbol{\sigma}'$ (regardless of ω). When the overall integral tends to zero, it means that the combined variations of the electromagnetic fields (represented by the vector and scalar potentials) do not cause significant changes in the perturbed energy functional. This behavior is fundamental for the stability of the system. In practical terms, if the overall integral expression approaches zero, it implies that the electromagnetic system is in a stable equilibrium state. Perturbations in the potentials do not cause substantial energy variations, indicating that the system returns to a state of minimum energy after a perturbation. This stability condition is crucial

to ensure that the numerical solutions obtained through discretization and analysis are reliable and accurately represent the physical behavior of the system. In other words, the fact that the integral tends to zero ensures that variations in the electromagnetic fields, due to defects or other perturbations, do not lead to instabilities or divergences in the calculations. This means that the method used to model and analyze the system is robust and that the solutions are physically meaningful.

Remark 15. *Although the coercivity of the energy functional indicates that it has a unique minimum and ensures numerical stability, it is still necessary to further evaluate stability for several reasons. Coercivity ensures stability under small perturbations, but it is critical to evaluate how sensitive the system is to these perturbations. Sensitivity analysis helps determine whether small changes in inputs or parameters can lead to significant variations in the solution, which could indicate potential instabilities in practical applications.*

Remark 16. *Numerical methods introduce approximation errors through discretization, and although the coercive functional guarantees theoretical stability, these errors can accumulate and affect the stability of the solution. Furthermore, nonlinearities and complex boundary conditions may mean that the coercive functional alone may not capture these peculiarities.*

Remark 17. *In practice, CFRPs present inhomogeneities and anisotropies which can influence the stability of the solution. Even with a coercive functional, it is important to evaluate how these material properties influence the overall stability and whether the numerical method can accurately account for them. Evaluating stability ensures that the chosen conditions do not lead to spurious oscillations, divergences, or other instabilities in the solution.*

11. Construction of a Numerical Approach

We discretize the EC problem starting from the energy functional. This is because, first, the energy functional is coercive, which means that it tends to penalize non-physical, unstable or oscillating solutions. This leads to numerically stable solutions. Furthermore, the energy-based formulation ensures that energy conservation laws are respected in the discrete model. Furthermore, boundary conditions are incorporated directly into the variational formulation, simplifying implementation compared to other methods where boundary conditions must be treated separately.

We use the finite element method (FEM) to discretize the functional spaces W and $H^1_{\#}(\Omega_C)$ [42,43]. Particularly, to represent $\mathbf{A}$, we use Nédélec elements because they, ensuring the that the tangential electric and magnetic fields are continuous across element edges, are particularly suitable for electromagnetic problems, since they respect the continuity of the curl and are well defined for $\mathbf{A}$. Nédélec elements are particularly well suited for the discretization of problems involving vector fields for maintaining the correct physical behavior of the problem, especially in the presence of anisotropic materials and complex domains. Additionally, the use of Nédélec elements guarantees an accurate representation of the curl ($\nabla\times$) and divergence ($\nabla\cdot$) of the fields, which are essential for preserving the conservation properties of the electromagnetic fields in the domain under consideration. While nodal Lagrange elements are commonly used in many $(\mathbf{A}, \phi)$ formulations of the EC model, as highlighted in the literature, the choice of Nédélec elements proves to be more appropriate for our specific case study, ensuring greater accuracy and numerical stability in solving the problem [42,43].

Remark 18. *The comparison between the energy functional and the perturbed energy functional highlights their advantages in different electromagnetic analysis contexts. The energy functional represents the total energy of the electromagnetic system, offering intrinsic stability due to its coercive nature, which guarantees a unique minimum and stable numerical solutions. It provides a global understanding of the system, encompassing all energy components without focusing on specific perturbations, making it general and versatile for a wide range of problems. In contrast, the perturbed energy functional is tailored for analyzing system perturbations, such as changes in conductivity.*

This functional is particularly useful for detecting material defects, as it directly accounts for specific perturbations, enhancing the precision of analyses where perturbations significantly impact the system. Additionally, it is flexible and can easily incorporate new types of perturbations or changes in system parameters.

With these purposed in mind, we require that the perturbed energy functional $\mathcal{E}_1^{\text{pert}}$ is stationary, i.e., its variations are zero, $\delta\mathcal{E}_1^{\text{pert}} = 0$. The stationary of $\mathcal{E}_1^{\text{pert}}$ means that the variation of the energy functional with respect to arbitrary variations of functions $\mathbf{A}_C$ and ϕ_C must be zero.

Here, ζ is an infinitesimally small parameter that measures the magnitude of variations $\delta\mathbf{A}_C$ and $\delta\phi_C$. For the stationary of the functional, this derivative must be zero for every admissible variation $(\delta\mathbf{A}_C, \delta\phi_C)$.

Remark 19. *$\mathcal{E}_1^{pert}$ depends on $\mathbf{A}_C$, ϕ_C, $\mathbf{v}$, and Φ_C. To find the equations that $\mathbf{A}_C$ and ϕ_C must satisfy, we consider the variation of the functional with respect to arbitrary variations of $\mathbf{A}_C$ and ϕ_C. Therefore, $\delta\mathcal{E}_1^{pert}[(\mathbf{A}_C, \phi_C), (\delta\mathbf{A}_C, \delta\phi_C)]$ specifically represents the change in functional $\mathcal{E}_1^{pert}$ due to small perturbations $(\delta\mathbf{A}_C, \delta\phi_C)$ around functions $(\mathbf{A}_C, \phi_C)$. This means we are looking at how $\mathcal{E}_1^{pert}$ changes when $\mathbf{A}_C$ is perturbed to $\mathbf{A}_C + \zeta\delta\mathbf{A}_C$ and ϕ_C is perturbed to $\phi_C + \zeta\delta\phi_C$.*

Therefore, we start from the stationary condition of the energy functional for the electromagnetic system with arbitrary variations, which requires finding $(\mathbf{A}_C, \phi_C)$ such that for every $(\delta\mathbf{A}_C, \delta\phi_C)$

$$\int_{\Omega_C} \left(\frac{1}{\mu}(\nabla \times \mathbf{A}_C) \cdot (\nabla \times \overline{\delta\mathbf{A}_C}) + j\omega\boldsymbol{\sigma}'\mathbf{A}_C \cdot \overline{\delta\mathbf{A}_C} + j\omega\boldsymbol{\sigma}'\nabla\phi_C \cdot \overline{\delta\mathbf{A}_C} + \right.$$
$$\left. + j\omega\boldsymbol{\sigma}'\mathbf{A}_C \cdot \nabla\overline{\delta\phi_C} + j\omega\boldsymbol{\sigma}'\nabla\phi_C \cdot \nabla\overline{\delta\phi_C} \right) d\Omega_C = 0. \tag{52}$$

We divide Ω_C into small finite elements Ω_C^e, so that the sum of the integrals over the elements Ω_C^e represents the integral over the entire domain Ω_C, $\int_{\Omega_C} = \sum_e \int_{\Omega_C^e}$. Thus, formulation (52) becomes

$$\sum_e \int_{\Omega_C^e} \left(\frac{1}{\mu}(\nabla \times \mathbf{A}_C) \cdot (\nabla \times \overline{\delta\mathbf{A}_C}) + j\omega\boldsymbol{\sigma}'\mathbf{A}_C \cdot \overline{\delta\mathbf{A}_C} + j\omega\boldsymbol{\sigma}'\nabla\phi_C \cdot \overline{\delta\mathbf{A}_C} + \right.$$
$$\left. + j\omega\boldsymbol{\sigma}'\mathbf{A}_C \cdot \nabla\overline{\delta\phi_C} + j\omega\boldsymbol{\sigma}'\nabla\phi_C \cdot \nabla\overline{\delta\phi_C} \right) d\Omega_C^e = 0. \tag{53}$$

To approximate $\mathbf{A}_C$ and ϕ_C as linear combinations of basis functions $\mathbf{N}_i$ and N_{ki}, we write

$$\mathbf{A}_C \approx \sum_{i=1}^{N} \mathbf{N}_i A_i, \tag{54}$$

and

$$\phi_C \approx \sum_{k=1}^{N} N_k \phi_k, \tag{55}$$

where $\mathbf{N}_i$ and N_k are the finite element shape functions, and A_i and ϕ_j are the expansion coefficients. Thus, from (54) and (55), we achieve $\delta\mathbf{A}_C \approx \sum_{i=1}^{N} \mathbf{N}_i \delta A_i$ and $\delta\phi_C \approx \sum_{k=1}^{N} N_k \delta\phi_k$. Therefore, the first term in (53), since

$$\nabla \times \left(\sum_{i=1}^{N} \mathbf{N}_i A_i \right) = \sum_{i=1}^{N} (\nabla \times \mathbf{N}_i) A_i \tag{56}$$

and

$$\nabla \times \left(\sum_{k=1}^{N} \overline{\mathbf{N}_k} \delta A_k \right) = \sum_{k=1}^{N} (\nabla \times \overline{\mathbf{N}_k}) \delta A_k, \tag{57}$$

becomes

$$\begin{aligned} &\int_{\Omega_C^e} \frac{1}{\mu} (\nabla \times \mathbf{A}_C) \cdot (\nabla \times \overline{\delta \mathbf{A}_C}) \, d\Omega_C^e \approx \\ &\approx \int_{\Omega_C^e} \frac{1}{\mu} \left(\nabla \times \sum_{i=1}^{N} \mathbf{N}_i A_i \right) \cdot \left(\nabla \times \sum_{k=1}^{N} \overline{\mathbf{N}_k} \delta A_k \right) d\Omega_C^e = \\ &= \int_{\Omega_C^e} \frac{1}{\mu} \left(\sum_{i=1}^{N} (\nabla \times \mathbf{N}_i) A_i \right) \cdot \left(\sum_{k=1}^{N} (\nabla \times \overline{\mathbf{N}_k}) \delta A_k \right) d\Omega_C^e. \end{aligned} \tag{58}$$

Furthermore, we have

$$\begin{aligned} &\left(\sum_{i=1}^{N} (\nabla \times \mathbf{N}_i) A_i \right) \cdot \left(\sum_{k=1}^{N} (\nabla \times \overline{\mathbf{N}_k}) \delta A_k \right) = \\ &= \sum_{i=1}^{N} \sum_{k=1}^{N} \left((\nabla \times \mathbf{N}_i) A_i \cdot (\nabla \times \overline{\mathbf{N}_k}) \delta A_k \right) = \sum_{i=1}^{N} \sum_{k=1}^{N} A_i (\nabla \times \mathbf{N}_i) \cdot (\nabla \times \overline{\mathbf{N}_k}) \delta A_k. \end{aligned} \tag{59}$$

Thus, integral (58) becomes

$$\begin{aligned} &\int_{\Omega_C^e} \frac{1}{\mu} (\nabla \times \mathbf{A}_C) \cdot (\nabla \times \overline{\delta \mathbf{A}_C}) \, d\Omega_C^e \approx \\ &\approx \int_{\Omega_C^e} \frac{1}{\mu} \sum_{i=1}^{N} \sum_{k=1}^{N} A_i (\nabla \times \mathbf{N}_i) \cdot (\nabla \times \overline{\mathbf{N}_k}) \delta A_k \, d\Omega_C^e = \\ &= \sum_{i=1}^{N} \sum_{k=1}^{N} A_i \delta A_k \int_{\Omega_C^e} \frac{1}{\mu} (\nabla \times \mathbf{N}_i) \cdot (\nabla \times \overline{\mathbf{N}_k}) \, d\Omega_C^e, \end{aligned} \tag{60}$$

which reduces to $\sum_{i=1}^{N} \sum_{k=1}^{N} K_{ik} A_i \delta A_k$, where $K_{ik} = \int_{\Omega_C^e} \frac{1}{\mu} (\nabla \times \mathbf{N}_i) \cdot (\nabla \times \overline{\mathbf{N}_k}) \, d\Omega_C^e$.

Considering the second term in (53), substituting in it the approximations, it is easy to achieve

$$\begin{aligned} \int_{\Omega_C^e} j\omega \boldsymbol{\sigma}' \mathbf{A}_C \cdot \overline{\delta \mathbf{A}_C} \, d\Omega_C^e &\approx \int_{\Omega_C^e} j\omega \boldsymbol{\sigma}' \left(\sum_{i=1}^{N} \mathbf{N}_i A_i \right) \cdot \left(\sum_{k=1}^{N} \overline{\mathbf{N}_k} \delta A_k \right) d\Omega_C^e = \\ &= \int_{\Omega_C^e} j\omega \boldsymbol{\sigma}' \sum_{i=1}^{N} \sum_{k=1}^{N} A_i \mathbf{N}_i \cdot \overline{\mathbf{N}_k} \delta A_k \, d\Omega_C^e = \\ &= \sum_{i=1}^{N} \sum_{k=1}^{N} A_i \delta A_k \int_{\Omega_C^e} j\omega \boldsymbol{\sigma}' \mathbf{N}_i \cdot \overline{\mathbf{N}_k} \, d\Omega_C^e = \sum_{i=1}^{N} \sum_{k=1}^{N} C_{ik} A_i \delta A_k, \end{aligned} \tag{61}$$

where $C_{ik} = \int_{\Omega_C} j\omega \boldsymbol{\sigma}' \mathbf{N}_i \cdot \overline{\mathbf{N}_k} \, d\Omega_C^e$. Similarly, for the third term, we have

$$\int_{\Omega_C^e} j\omega\boldsymbol{\sigma}'\nabla\phi_C\cdot\overline{\delta\mathbf{A}_C}\,d\Omega_C^e \approx \int_{\Omega_C^e} i\omega\boldsymbol{\sigma}'\left(\nabla\sum_{i=1}^{N}N_i\phi_i\right)\cdot\left(\sum_{k=1}^{N}\overline{\mathbf{N}_k}\delta A_k\right)d\Omega_C^e = \\ = \int_{\Omega_C} i\omega\boldsymbol{\sigma}'\sum_{i=1}^{N}\sum_{k=1}^{N}\phi_i(\nabla N_i)\cdot\overline{\mathbf{N}_k}\delta A_k\,d\Omega_C^e = \\ = \sum_{i=1}^{N}\sum_{k=1}^{N}\phi_i\delta A_k\int_{\Omega_C^e} j\omega\boldsymbol{\sigma}'(\nabla N_i)\cdot\overline{\mathbf{N}_k}\,d\Omega_C^e = \sum_{i=1}^{N}\sum_{k=1}^{N}Q_{ik}\phi_i\delta A_k, \tag{62}$$

where $Q_{ik} = \int_{\Omega_C^e} j\omega\boldsymbol{\sigma}'(\nabla N_i)\cdot\overline{\mathbf{N}_k}\,d\Omega_C^e$. The same procedure, applied to the fourth term, provides

$$\int_{\Omega_C} j\omega\boldsymbol{\sigma}'\mathbf{A}_C\cdot\nabla\overline{\delta\phi_C}\,d\Omega_C \approx \int_{\Omega_C^e} j\omega\boldsymbol{\sigma}'\left(\sum_{i=1}^{N}\mathbf{N}_iA_i\right)\cdot\left(\nabla\sum_{k=1}^{N}\overline{N_k}\delta\phi_k\right)d\Omega_C^e = \\ = \int_{\Omega_C^e} j\omega\boldsymbol{\sigma}'\sum_{i=1}^{N}\sum_{k=1}^{N}A_i\mathbf{N}_i\cdot(\nabla\overline{N_k})\delta\phi_k\,d\Omega_C^e = \\ = \sum_{i=1}^{N}\sum_{k=1}^{N}A_i\delta\phi_k\int_{\Omega_C^e} j\omega\boldsymbol{\sigma}'\mathbf{N}_i\cdot(\nabla\overline{N_k})\,d\Omega_C^e = \sum_{i=1}^{N}\sum_{k=1}^{N}E_{ik}A_i\delta\phi_k, \tag{63}$$

in which $E_{ik} = \int_{\Omega_C^e} j\omega\boldsymbol{\sigma}'\mathbf{N}_i\cdot(\nabla\overline{N_k})\,d\Omega_C^e$. Finally, the fifth can be written as follows:

$$\int_{\Omega_C} j\omega\boldsymbol{\sigma}'\nabla\phi_C\cdot\nabla\overline{\delta\phi_C}\,d\Omega_C \approx \int_{\Omega_C^e} j\omega\boldsymbol{\sigma}'\left(\nabla\sum_{i=1}^{N}N_i\phi_i\right)\cdot\left(\nabla\sum_{k=1}^{N}\overline{N_k}\delta\phi_k\right)d\Omega_C^e = \\ = \int_{\Omega_C^e} j\omega\boldsymbol{\sigma}'\sum_{i=1}^{N}\sum_{k=1}^{N}\phi_i(\nabla N_i)\cdot(\nabla\overline{N_k})\delta\phi_k\,d\Omega_C^e = \\ = \sum_{i=1}^{N}\sum_{k=1}^{N}\phi_i\delta\phi_k\int_{\Omega_C^e} j\omega\boldsymbol{\sigma}'(\nabla N_i)\cdot(\nabla\overline{N_k})\,d\Omega_C^e = \sum_{i=1}^{N}\sum_{k=1}^{N}F_{ik}\phi_j\delta\phi_k, \tag{64}$$

where $F_{ik} = \int_{\Omega_C^e} j\omega\boldsymbol{\sigma}'(\nabla N_i)\cdot(\nabla\overline{N_k})\,d\Omega_C^e$.

Then, adding all the terms, we obtain

$$\sum_{i=1}^{N}\sum_{k=1}^{N}K_{ik}A_i\delta A_k + \sum_{i=1}^{N}\sum_{k=1}^{N}C_{ik}A_i\delta A_k + \sum_{i=1}^{N}\sum_{k=1}^{N}Q_{ik}\phi_i\delta A_k + \\ + \sum_{i=1}^{N}\sum_{k=1}^{N}E_{ik}A_i\delta\phi_k + \sum_{i=1}^{N}\sum_{k=1}^{N}F_{ik}\phi_i\delta\phi_k = 0, \tag{65}$$

from which, collecting similar terms,

$$\sum_{i=1}^{N}\sum_{k=1}^{N}(K_{ik}+C_{ik})A_i\delta A_k + \sum_{i=1}^{N}\sum_{k=1}^{N}Q_{ik}\phi_j\delta A_k + \sum_{i=1}^{N}\sum_{k=1}^{N}E_{ik}A_i\delta\phi_k + \sum_{i=1}^{N}\sum_{k=1}^{N}F_{ik}\phi_i\delta\phi_k = 0. \tag{66}$$

Now, arranging (66), we obtain

$$\delta\mathbf{A}[(\mathbf{K}+\mathbf{C})\mathbf{A}+\mathbf{Q}\boldsymbol{\phi}] + \delta\boldsymbol{\phi}[\mathbf{E}\mathbf{A}+\mathbf{F}\boldsymbol{\phi}] = 0 \tag{67}$$

in which the matrices are defined as follows:

$$\mathbf{K}_{ik} = \int_{\Omega_C}\frac{1}{\mu}(\nabla\times\mathbf{N}_i)\cdot(\nabla\times\mathbf{N}_k)\,d\Omega_C, \quad \mathbf{C}_{ik} = \int_{\Omega_C} j\omega\boldsymbol{\sigma}'\mathbf{N}_i\cdot\mathbf{N}_k\,d\Omega_C, \tag{68}$$

$$\mathbf{Q}_{ik} = \int_{\Omega_C} j\omega\boldsymbol{\sigma}'(\nabla N_i)\cdot\mathbf{N}_k\, d\Omega_C, \quad \mathbf{E}_{ik} = \int_{\Omega_C} j\omega\boldsymbol{\sigma}'\mathbf{N}_i\cdot(\nabla N_k)\, d\Omega_C, \tag{69}$$

$$\mathbf{F}_{ik} = \int_{\Omega_C} j\omega\boldsymbol{\sigma}'(\nabla N_i)\cdot(\nabla N_k)\, d\Omega_C. \tag{70}$$

Moreover, $\mathbf{A} = \begin{bmatrix} A_1 & A_2 & \dots & A_N \end{bmatrix}^T$, while $\boldsymbol{\phi} = \begin{bmatrix} \phi_1 & \phi_2 & \dots & \phi_N \end{bmatrix}^T$.

Matrix $\mathbf{K}$ represents the stiffness matrix from the discretization of the curl of vector potential $\mathbf{A}_C$. It accounts for the magnetic properties of the material and is associated with the magnetic energy stored due to EC. Matrix $\mathbf{C}$ is the coupling matrix between vector potential $\mathbf{A}_C$ and electrical conductivity $\boldsymbol{\sigma}'$. It accounts for the Joule losses caused by induced currents, describing the interaction between the magnetic field and the conductive response of the material. Matrix $\mathbf{Q}$ involves the scalar potential ϕ_C and the vector potential $\mathbf{A}_C$. It represents the effect of the electric potential distribution on the magnetic field, describing how variations in the electric potential influence induced currents and the magnetic field. Matrix $\mathbf{E}$ represents the coupling between the vector potential $\mathbf{A}_C$ and the gradient of the scalar potential ϕ_C. It describes how the induced magnetic field affects the electric potential distribution within the material, indicating the interaction between the magnetic field and the electric field. Matrix $\mathbf{F}$ involves the gradient of the scalar potential ϕ_C. It accounts for electrical conductivity $\boldsymbol{\sigma}'$ and describes how the electric field is distributed within the material, representing the stored electric energy and the Joule losses associated with electric potential distribution.

It is worth noting that (67) can be written as

$$\begin{bmatrix}\delta\mathbf{A} & \delta\boldsymbol{\phi}\end{bmatrix}\begin{bmatrix}(\mathbf{K}+\mathbf{C})\mathbf{A}+\mathbf{Q}\boldsymbol{\phi} \\ \mathbf{E}\mathbf{A}+\mathbf{F}\boldsymbol{\phi}\end{bmatrix} = \begin{bmatrix}\delta\mathbf{A} & \delta\boldsymbol{\phi}\end{bmatrix}\begin{bmatrix}(\mathbf{K}+\mathbf{C}) & \mathbf{Q} \\ \mathbf{E} & \mathbf{F}\end{bmatrix}\begin{bmatrix}\mathbf{A} \\ \boldsymbol{\phi}\end{bmatrix} = 0. \tag{71}$$

Therefore, indicating by

$$\mathbf{x} = \begin{bmatrix}\mathbf{A} \\ \boldsymbol{\phi}\end{bmatrix}, \quad \delta\mathbf{x} = \begin{bmatrix}\delta\mathbf{A} \\ \delta\boldsymbol{\phi}\end{bmatrix}, \quad \mathbf{M} = \begin{bmatrix}(\mathbf{K}+\mathbf{C}) & \mathbf{Q} \\ \mathbf{E} & \mathbf{F}\end{bmatrix}, \tag{72}$$

Equation (71) becomes $\delta\mathbf{x}^T\mathbf{M}\mathbf{x} = 0$. Therefore, for in all variations $\delta\mathbf{X}$, it must be:

$$\mathbf{M}\mathbf{x} = \begin{bmatrix}(\mathbf{K}+\mathbf{C}) & \mathbf{Q} \\ \mathbf{E} & \mathbf{F}\end{bmatrix}\begin{bmatrix}\mathbf{A} \\ \boldsymbol{\phi}\end{bmatrix} = 0, \tag{73}$$

which represents a system of algebraic equations to be solved numerically.

12. On the Solution of the Algebraic System

To capture even the smallest imperfections in the material, it is necessary to prepare a rather fine spatial discretization of the domain. This implies that the resolution of the algebraic system must be addressed using a computationally suitable approach. In this paper, we use a Preconditioned Conjugate Gradient (PCG) approach [43].

12.1. Preconditioned Conjugate Gradient (PCG) Method

Using the MATLAB *isequal* subroutine, we verified that matrix $\mathbf{M}$ is equal to its conjugate transpose. Furthermore, the *eig* subroutine allowed us to verify that the eigenvalues of $\mathbf{M}$ are all positive. It follows that $\mathbf{M}$ is positive definite, so PCG can be applied exploiting an invertible $\mathbf{P}$ preconditioner to improve convergence. We set an initial vector $\mathbf{x}_0$ as a null vector to then calculate the initial residual $\mathbf{r}_0 = \mathbf{b} - \mathbf{M}\mathbf{x}_0$, where $\mathbf{b}$ is usually the vector of any known terms. The procedure requires solving $\mathbf{P}\mathbf{z}_0 = \mathbf{r}_0$ to obtain $\mathbf{z}_0$, and then setting the initial direction vector $\mathbf{p}_0 = \mathbf{z}_0$. Then, at each iteration k, the parameter is calculated,

$$\alpha_k = \frac{\mathbf{r}_k^T\mathbf{z}_k}{\mathbf{p}_k^T\mathbf{M}\mathbf{p}_k} \tag{74}$$

which allows the following update of the solution, $\mathbf{x}_{k+1} = \mathbf{x}_k + \alpha_k \mathbf{p}_k$, and the residue, $\mathbf{r}_{k+1} = \mathbf{r}_k - \alpha_k \mathbf{M}\mathbf{p}_k$. If $\|\mathbf{r}_{k+1}\|$ is less than a predefined tolerance, the iteration stops. Then, the preconditioned system is solved, $\mathbf{P}\mathbf{z}_{k+1} = \mathbf{r}_{k+1}$, by which the followimng ca be calculated:

$$\beta_k = \frac{\mathbf{r}_{k+1}^T \mathbf{z}_{k+1}}{\mathbf{r}_k^T \mathbf{z}_k}, \tag{75}$$

used to update the descent direction vector, $\mathbf{p}_{k+1} = \mathbf{z}_{k+1} - \beta_k \mathbf{p}_k$. The entire procedure repeats until convergence, or until the maximum number of iterations is reached [43].

12.2. Construction of the Preconditioner

The Cholesky preconditioner is used to improve the convergence of the PCG method. It is based on the Cholesky decomposition of preconditioner $\mathbf{P}$. To address efficiency, we use the incomplete Cholesky decomposition which approximates $\mathbf{P}$ as $\mathbf{P} \approx \mathbf{L}\mathbf{L}^*$, where $\mathbf{L}$ is a lower triangular matrix with positive diagonal elements and $\mathbf{L}^*$ is the transpose conjugate of $\mathbf{L}$. To calculate all the elements of $\mathbf{L}$, we use the Cholesky Banachiewicz algorithm which determines the elements of the lower triangular matrix as follows:

$$L_{ii} = \sqrt{M_{ii} - \sum_{k=1}^{i-1} L_{ik}^2} \quad \text{(diagonal elements)}, \tag{76}$$

$$L_{ij} = \frac{1}{L_{jj}} \left(M_{ij} - \sum_{i=1}^{j-1} L_{ii} L_{ji} \right) \quad \text{(elements below the diagonal)} \tag{77}$$

retaining only a part of the non-zero elements of $\mathbf{L}$. This reduces the number of computations and memory requirements. This preconditioner is used to transform the original system $\mathbf{M}\mathbf{x} = \mathbf{b}$ into a preconditioned system $\mathbf{P}^{-1}\mathbf{M}\mathbf{x} = \mathbf{P}^{-1}\mathbf{b}$, which has better convergence properties (for details, see [43]).

Remark 20. *The Cholesky preconditioner combined with the conjugate gradient method was used rather than a direct solver, both for problems of computational efficiency and for memory management (linked to the fact that the algebraic system obtained is large with matrices sparse defined positive). We observe that the use of a direct solver (e.g., direct Cholesky factorization) can be computationally expensive, given the number of arithmetic operations required, often producing dense matrices. Obviously, to avoid problems of bad conditioning of the matrix, a Cholesky preconditioner was used (which preserves the sparse structure of the matrix), making the iterative solver more stable and also accelerating convergence [43].*

Remark 21. *The accuracy of the iterative method compared to the direct method was evaluated through a detailed analysis which involved both the comparison of the solutions obtained in terms of relative errors and the monitoring of convergence through the residual norm. To measure the relative error between the solutions, we compared the exact solution, obtained with the direct solver via Cholesky factorization, with the approximate solution, derived from the use of the preconditioned iterative method. The analysis strongly suggested that the resulting relative error was acceptable, indicating that the iterative solution was very close to that obtained with the direct method. This result confirms that despite the approximate nature of the iterative method, the quality of the solution is adequate for the needs of the problem addressed, and the iterative approach is capable of providing results that are significantly close to the exact solution.*

Remark 22. *Krylov subspace methods [44] are popular for solving large sparse linear systems, but they were not used in this study for several reasons. These methods are useful for non-symmetric or indefinite matrices, whereas our matrix is symmetric and positive definite, making the PCG method more natural and efficient. Moreover, the PCG method, with appropriate preconditioning, converges faster for large, sparse, and well-conditioned systems. The structure of the problem allows*

the PCG method to fully exploit the properties of the matrix, improving performance in terms of computational resources and convergence rates.

13. Error Estimation

13.1. An Estimate of the Error in $H(curl, \Omega_C)$

13.1.1. Definition of the Finite Element Space V_h

Space V_h is defined as the set of vector functions that can be expressed as linear combinations of the Nedelec finite element shape functions. Formally, for a discretization with elements of order p, space V_h is given by

$$V_h = \left\{ \mathbf{v}_h \in H(\text{curl}, \Omega_C) \mid \mathbf{v}_h|_K \in \mathcal{P}_p(K) \text{ for every finite element } K \subset \Omega_C \right\}, \quad (78)$$

where $\mathcal{P}_p(K)$ represents the space of polynomials of degree p on a finite element K. Nedelec elements are particularly suitable because they ensure the continuity of the tangential components of the vector field between finite elements. Moreover, their formulation accurately represents the curl of the vector field, improving the precision in solving Maxwell's equations. Finally, they are very suitable for complex domains and irregular geometries, maintaining discretization accuracy [43].

To obtain an error estimate for $\mathbf{A}_C$, we use the well-known result from finite element theory, according to which

$$\|\mathbf{e}_\mathbf{A}\|_{H(\text{curl},\Omega_C)} \leq C \left(\inf_{\mathbf{v}_h \in V_h} \|\mathbf{A}_C - \mathbf{v}_h\|_{H(\text{curl},\Omega_C)} \right), \quad (79)$$

where C is a problem-dependent constant.

13.1.2. Nedelec Element Approximation Properties

The Nedelec elements of order p have approximation properties which guarantee that for every sufficiently regular function $\mathbf{A}_C \in H^{p+1}(\Omega_C)$, there exists a $\mathbf{v}_h \in V_h$ such that

$$\|\mathbf{A}_C - \mathbf{v}_h\|_{H(\text{curl},\Omega_C)} \leq C_1 h^p \|\mathbf{A}_C\|_{H^{p+1}(\Omega_C)}, \quad (80)$$

where C_1 is a constant depending on the shape of the finite elements and on the regularity of the exact solution and

$$H^{p+1}(\Omega_C) = \left\{ \mathbf{v} \in L^2(\Omega_C) \mid D^\alpha \mathbf{v} \in L^2(\Omega_C) \forall \text{ multi-indices } \alpha \text{ with } |\alpha| \leq p+1 \right\}, \quad (81)$$

where D^α denotes the weak derivative corresponding to the multi-index α; C_1 is a constant that depends on the shape and quality of the finite elements and the regularity of the exact solution. Finally, combining the estimates above, we obtain

$$\|\mathbf{e}_\mathbf{A}\|_{H(\text{curl},\Omega_C)} \leq C \left(C_1 h^p \|\mathbf{A}_C\|_{H^{p+1}(\Omega_C)} \right) = C_1' h^p \|\mathbf{A}_C\|_{H^{p+1}(\Omega_C)}, \quad (82)$$

where $C_1' = C \cdot C_1$ is a new constant.

Remark 23. *Sobolev space $H^{p+1}(\Omega_C)$ is critical in the context of finite element methods because it characterizes the regularity of the exact solution. Functions in $H^{p+1}(\Omega_C)$ have sufficient smoothness, allowing for higher-order derivatives to exist in the L^2 sense. Degree $p+1$ indicates the level of derivative that needs to be square-integrable, and this level of regularity is directly related to the convergence rate of the finite element approximation.*

13.1.3. Significance of h

h is defined as the maximum length of the edges of the finite elements in domain Ω_C. Mathematically, for a tetrahedral finite element, h can be defined as $h = \max_{e \in E} \text{length}(e)$,

where E is the set of edges of the finite element. Additionally, the mesh size $h(T_k)$ can be defined as the diameter of the element T_k:

$$h(T_k) = \text{diameter}(T_k) = \sup_{x,y \in T_k} \|x - y\|, \tag{83}$$

and the characteristic dimension h of the mesh is given by $h = \max_{T_k \in T} h(T_k)$, where T is the set of all finite elements in domain Ω_C and T_k is a single finite element in the domain. Thus, h represents the maximum size of the finite elements used to discretize the domain. The error estimate shows that the discretization error $\|\mathbf{e_A}\|_{H(\text{curl},\Omega_C)}$ is proportional to h^p, where p is the order of the polynomials used in the Nedelec finite element shape functions. Consequently, reducing h (i.e., using a finer mesh) decreases the error, improving the accuracy of the numerical solution. This highlights the importance of a well-refined mesh to achieve precise results in electromagnetic problems.

13.2. An Estimate of the Error in $H^1(\Omega_C)$

As in the previous case, we use the following result:

$$\|e_\phi\|_{H^1(\Omega_C)} \leq C\left(\inf_{v_h \in W_h} \|\phi_C - v_h\|_{H^1(\Omega_C)}\right), \tag{84}$$

where C is a problem-dependent constant and W_h denotes the finite element space for ϕ_C.

13.2.1. Finite Element Space for ϕ_C

W_h is defined as follows:

$$W_h = \left\{v_h \in H^1(\Omega_C) \mid v_h|_K \in \mathcal{P}_p(K) \text{ for every finite element } K \subset \Omega_C\right\}, \tag{85}$$

where $\mathcal{P}_p(K)$ represents the space of polynomials of degree p on a finite element K.

13.2.2. Finite Element Approximation Properties for ϕ_C

The finite elements of order p have approximation properties which guarantee that for every sufficiently regular function $\phi_C \in H^{p+1}(\Omega_C)$, there exists a $v_h \in W_h$ such that

$$\|\phi_C - v_h\|_{H^1(\Omega_C)} \leq C_1 h^p \|\phi_C\|_{H^{p+1}(\Omega_C)}. \tag{86}$$

Therefore, combining the estimates, we can easily write

$$\|e_\phi\|_{H^1(\Omega_C)} \leq C\left(C_1 h^p \|\phi_C\|_{H^{p+1}(\Omega_C)}\right) = C_1' h^p \|\phi_C\|_{H^{p+1}(\Omega_C)}, \tag{87}$$

where $C_1' = C \cdot C_1$ is a new constant that encapsulates the dependencies on both the problem and the finite element characteristics. The error estimate in the $H^1(\Omega_C)$ norm for the finite element method shows that the error scales with mesh size h to the power of polynomial degree p, and it is influenced by a constant related to the regularity of the exact solution and the quality of the finite elements. This emphasizes the necessity of selecting appropriate polynomial degrees and ensuring high-quality mesh elements to obtain precise numerical solutions.

13.3. On the Procedure for Obtaining Triangulation

To develop the Delaunay triangulation mathematically, we start by defining a set of points P in the two-dimensional plane. The Delaunay triangulation is a triangulation such that no point in P lies inside the circumcircle of any triangle in the triangulation, thus maximizing the minimum angle of all triangles. The process begins with the creation of a supertriangle large enough to contain all points in P. Next, we insert each point p_i one at a time into the current triangulation. We find the triangle that contains p_i and split this

triangle into three new triangles, updating the triangulation. After each insertion, we check that the triangles satisfy the Delaunay criterion: if a triangle does not meet this criterion, we perform an edge flip, replacing the non-conforming edge with the other edge that divides the four involved points. By continuing this process for all points, we obtain a triangulation that satisfies the Delaunay criterion. Finally, we remove the triangles that share vertices with the initial supertriangle. This method ensures a high-quality triangulation, which is crucial for accuracy and stability in numerical simulations, such as those used for analyzing electromagnetic fields in composite materials.

14. Numerical Simulation and Results

The proposed numerical procedure was implemented on a high-performance workstation with a 3.3 GHz Intel Core 2 CPU for MATLAB R2023b ToolBox simulations. This setup effectively handled large datasets and complex algorithms, ensuring fast execution and enabling comprehensive parameter analysis in a reasonable time.

14.1. The Domain under Study

In this study, we developed a detailed 3D model of a depth rudder using MATLAB® R2023b tailored to represent a component typically found in modern commercial airliners. The model meticulously delineates the depth rudder's geometric dimensions, with a height of 10 m, a width at the base of 2 m, and a thickness of 0.5 m, as shown in Figure 4a. These dimensions were chosen to reflect common specifications for large, long-range aircraft, akin to those used in transatlantic flights. The depth rudder is designed with a symmetrical airfoil shape to optimize aerodynamic efficiency and control stability at various flight speeds. This design is crucial for ensuring effective maneuverability and safety during critical flight operations such as takeoff, cruising, and landing. A Fluxset type EC probe (whose geometric characteristics of the probe and the E-shaped core are summarized in Tables 1 and 2, respectively) was simulated to scan the study area by simulating a step-by-step scanning system both along the width and along the height (see Figure 4b,c).

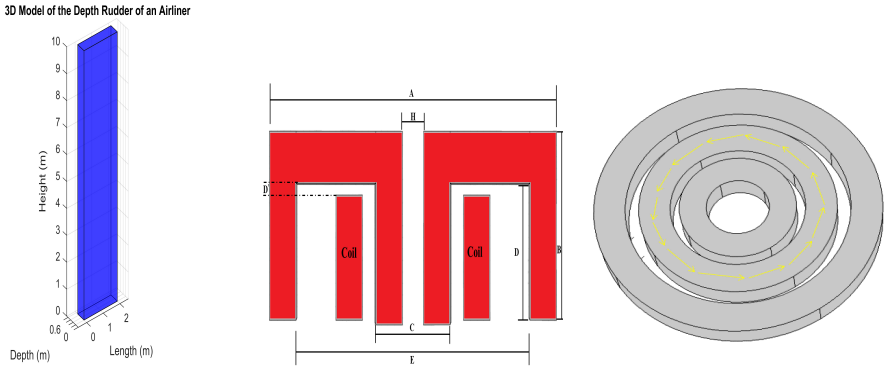


Figure 4. (**a**) Three-dimensional representation of an airliner's depth rudder modeled in MATLAB®, tailored for scenarios with minimal delamination influence conductivity. The model meticulously outlines the rudder's geometric dimensions, including height, width, and depth, ensuring precise detection of subtle conductivity changes. (**b**) Probe configuration for EC analysis and (**c**) a typical section view.

Table 1. Geometric characteristics of the coil.

External Diameter	Internal Diameter	Height	Number of Turns	Lift-Off
56 mm	54 mm	32 mm	1200	0.05 mm

Table 2. Geometric characteristics of the E-shaped core.

F	E	A	B	D	D′	H
54 mm	58 mm	511 mm	55.25 mm	53.5 mm	51.5 mm	52 mm

14.2. External Excitation Source and Frequency

From an electrical perspective, as in [9], the domain under study was subjected to a $\mathbf{J}_e = J_0 = e^{j\omega t}\hat{\theta}$ where J_0 = 110 mA/m^2 is the density magnitude of current and $\hat{\theta}$ is the unit vector in the azimuthal direction. In Cartesian coordinates, using $y(\sqrt{x^2+y^2})^{-1}$ and $\cos(\theta) = x(\sqrt{x^2+y^2})^{-1}$, we can write

$$\mathbf{J}_e(x,y,t) = J_0 e^{j\omega t}\left(-\frac{y}{\sqrt{x^2+y^2}}\hat{x} + \frac{x}{\sqrt{x^2+y^2}}\hat{y}\right) \tag{88}$$

where $\theta = \arctan\left(\frac{y}{x}\right)$, with frequency $f = 1.05MHz$ deemed necessary to highlight subsurface defects. This formulation, as required, ensures that $\nabla \cdot \mathbf{J}_e = 0$. $\mathbf{J}_e = J_0 e^{j\omega t}\hat{\theta}$ is particularly significant for CFRP materials because it considers both orthotropy and anisotropy characteristic of CFRPs [9]. Furthermore, the Cartesian decomposition (88) illustrates how the field varies spatially depending on the position in the material. The importance of considering both the orthotropy and anisotropy of CFRP materials is that these materials, used extensively in the aviation industry and other advanced applications, have mechanical and electrical properties that vary significantly depending on direction. Therefore, correct modeling must take these variations into account to accurately predict the behavior of the material under different operating conditions.

15. Convergence Analysis

From (82) and (87), considering two mesh sizes h_1 and h_2, with $h_1 > h_2$, we can easily write

$$\frac{\|\mathbf{e}_{\mathbf{A}}^{h_1}\|_{H(\mathrm{curl},\Omega_C)}}{\|\mathbf{e}_{\mathbf{A}}^{h_2}\|_{H(\mathrm{curl},\Omega_C)}} \approx \frac{h_1^{p_{\mathbf{A}}}}{h_2^{p_{\mathbf{A}}}}, \qquad \frac{\|e_{\phi}^{h_1}\|_{H^1(\Omega_C)}}{\|e_{\phi}^{h_2}\|_{H^1(\Omega_C)}} \approx \frac{h_1^{p_{\phi}}}{h_2^{p_{\phi}}} \tag{89}$$

where $\|\mathbf{e}_{\mathbf{A}}^{h_1}\|_{H(\mathrm{curl},\Omega_C)}$, $\|\mathbf{e}_{\mathbf{A}}^{h_1}\|_{H(\mathrm{curl},\Omega_C)}$, $\|\mathbf{e}_{\phi}^{h_1}\|_{H^1(\Omega_C)}$ and $\|\mathbf{e}_{\phi}^{h_2}\|_{H^1(\Omega_C)}$ represent the error estimates for $\mathbf{A}_C$ and ϕ_C at different values of h_1 and h_2, respectively. Therefore, from (89), applying the logarithmic operator on both sides, we obtain

$$p_{\mathbf{A}} \approx \frac{\log\left\{\frac{\|\mathbf{e}_A^{h_1}\|_{H(\mathrm{curl},\Omega_C)}}{\|\mathbf{e}_A^{h_2}\|_{H(\mathrm{curl},\Omega_C)}}\right\}}{\log\left(\frac{h_1}{h_2}\right)}, \qquad p_{\phi} \approx \frac{\log\left\{\frac{\|e_{\phi}^{h_1}\|_{H^1(\Omega_C)}}{\|e_{\phi}^{h_2}\|_{H^1(\Omega_C)}}\right\}}{\log\left(\frac{h_1}{h_2}\right)} \tag{90}$$

which represents the convergence rates (i.e., they measure how quickly the error between the numerical and exact solution decreases as the mesh resolution increases).

16. Numerical Simulations

16.1. Quantitative Analysis of Structural Defects: Scaling Factors α, β, γ, and δ in Modelling the Impact on Material Conductivity and Mechanical Properties

Parameters α and β quantify the impacts of delamination and microcracks, respectively, on the structure and electrical conductivity of materials. Both serve as scaling factors: values close to zero indicate the preservation of the material's original properties, while values near unity signal significant degradation due to the pronounced presence of delamination or microcracks, resulting in reduced conductivity. Similarly, parameters γ and δ could represent the influence of other structural defects or variations in physical properties,

essential for modeling the overall impact of various defects on material performance and developing appropriate mitigation strategies.

16.2. Mesh Setting

For each defect, including the concomitance of all defects, a considerable number of numerical simulations were performed for increasing values of h_i, $i = 1, 2, \ldots, 500$ to select the mesh with the best performances. In particular, for each simulation, $\|\mathbf{e_A}\|_{H(\mathrm{curl},\Omega_C)}$ and $\|e_\phi\|_{H^1(\Omega_C)}$ were evaluated (the exact solutions were obtained using the commercial software MAPLE 2021. The obtained convergence rates, as formulated in (90), were compared with the theoretical convergence rates predicted by the a priori error estimate: the best mesh is the one for which the calculated convergence rates are close to p.

16.3. Link between Quantitative Parameters of Defects with Degree of Freedom

Tables 3 and 4 present $\|\mathbf{e_A}\|_{H(\mathrm{curl},\Omega_C)}$ and $\|e_\phi\|_{H^1(\Omega_C)}$ as α, β, γ and δ increase, highlighting that as the magnitude of each defect increases, the required degrees of freedom (d.o.f.) decrease. This is mainly because, to detect large defects, it is not necessary to use refined meshes. However, in these cases, despite not requiring extremely dense meshes, the error increases: this should not worry us because even if the error begins to be significant, the size of the defect is such as to make it necessary to replace the benchmark. Obviously, common sense guides us: we consider a single mesh for all defects capable of detecting even small defects. Figure 5a displays this mesh, which thickens near the attachment points of the tail rudder to the fuselage. Furthermore, Tables 5 and 6 highlight the performance of the iterative solver as the type and extent of the defect vary. The analysis of the obtained results highlights the excellent performance both in terms of the number of iterations and in terms of accuracy compared to the use of the direct solver. As expected, defects apart from delamination require greater computational effort.

Table 3. $\|\mathbf{e_A}\|_{H(\mathrm{curl},\Omega_C)}$ and $\|e_\phi\|_{H^1(\Omega_C)}$ as both α and β increase.

α	d.o.f.	$\|\mathbf{e_A}\|_{H(\mathrm{curl},\Omega_C)}$	$\|e_\phi\|_{H^1(\Omega_C)}$	β	d.o.f.	$\|\mathbf{e_A}\|_{H(\mathrm{curl},\Omega_C)}$	$\|e_\phi\|_{H^1(\Omega_C)}$
0.1	91024	0.00591	0.0096	0.1	91024	0.00492	0.0096
0.2	89532	0.00615	0.0123	0.2	89532	0.00508	0.0104
0.3	88449	0.00686	0.0129	0.3	88449	0.00536	0.0129
0.4	87931	0.00743	0.0245	0.4	87931	0.00571	0.0185
0.5	86745	0.00819	0.0277	0.5	86745	0.00590	0.0210
0.6	85983	0.00887	0.0311	0.6	85983	0.00617	0.0235
0.7	82976	0.00909	0.0359	0.7	82976	0.00647	0.0267
0.8	79863	0.00155	0.0483	0.8	79863	0.00759	0.0291
0.9	78041	0.00126	0.0566	0.9	78041	0.00985	0.0308
1	74536	0.00994	0.0704	1	74536	0.00999	0.0357

Table 4. $\|\mathbf{e_A}\|_{H(\mathrm{curl},\Omega_C)}$ and $\|e_\phi\|_{H^1(\Omega_C)}$ as both γ and δ increase.

γ	d.o.f.	$\|\mathbf{e_A}\|_{H(\mathrm{curl},\Omega_C)}$	$\|e_\phi\|_{H^1(\Omega_C)}$	δ	d.o.f.	$\|\mathbf{e_A}\|_{H(\mathrm{curl},\Omega_C)}$	$\|e_\phi\|_{H^1(\Omega_C)}$
0.1	91024	0.00579	0.0094	0.1	91024	0.00512	0.0090
0.2	89532	0.00586	0.0120	0.2	89532	0.00531	0.0099
0.3	88449	0.00594	0.0131	0.3	88449	0.00579	0.0122
0.4	87931	0.00601	0.0159	0.4	87931	0.00613	0.0139
0.5	86745	0.00620	0.0177	0.5	86745	0.00634	0.0158
0.6	85983	0.00644	0.0186	0.6	85983	0.00699	0.0183
0.7	82976	0.00693	0.0192	0.7	82976	0.00734	0.0207
0.8	79863	0.00722	0.0209	0.8	79863	0.00786	0.0235
0.9	78041	0.00769	0.0235	0.9	78041	0.00841	0.0266
1	74536	0.00833	0.0257	1	74536	0.00906	0.0286

Table 5. Performance of the iterative solver as both α and β increase.

α	♯Iteration	Relative Error (%)	β	♯Iteration	Relative Error (%)
0.1	45	10^{-4}	0.1	46	10^{-4}
0.2	42	10^{-4}	0.2	41	10^{-4}
0.3	37	10^{-5}	0.3	39	10^{-5}
0.4	29	10^{-5}	0.4	27	10^{-6}
0.5	22	10^{-6}	0.5	23	10^{-6}
0.6	18	10^{-6}	0.6	17	10^{-6}
0.7	17	10^{-7}	0.7	15	10^{-7}
0.8	14	10^{-7}	0.8	11	10^{-7}
0.9	12	10^{-7}	0.9	9	10^{-7}
1	9	10^{-8}	1	7	10^{-7}

Table 6. Performance of the iterative solver as both γ and δ increase.

γ	♯Iteration	Relative Error (%)	δ	♯Iteration	Relative Error (%)
0.1	51	10^{-4}	0.1	54	10^{-4}
0.2	46	10^{-4}	0.2	44	10^{-4}
0.3	44	10^{-5}	0.3	40	10^{-5}
0.4	41	10^{-5}	0.4	36	10^{-5}
0.5	37	10^{-5}	0.5	34	10^{-5}
0.6	34	10^{-6}	0.6	30	10^{-6}
0.7	30	10^{-6}	0.7	25	10^{-6}
0.8	28	10^{-6}	0.8	19	10^{-7}
0.9	19	10^{-6}	0.9	17	10^{-7}
1	14	10^{-7}	1	16	10^{-7}

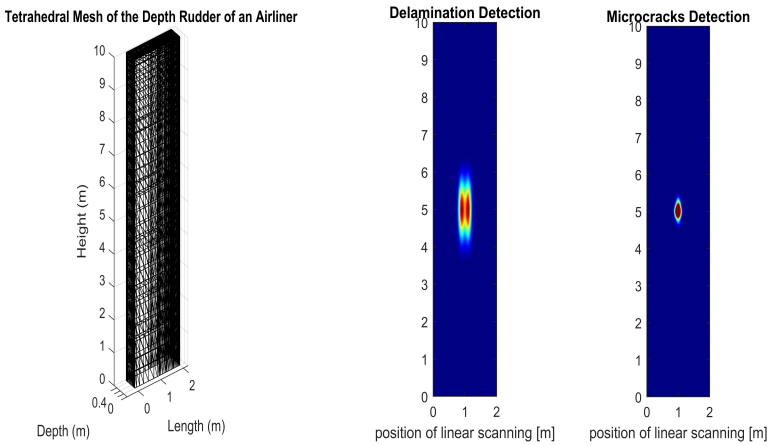


Figure 5. (**a**) Three-dimensional visualization of a depth rudder mesh model, featuring an irregular tetrahedral mesh with enhanced densification. This finely tuned mesh is critical for accurately capturing the smallest variations in conductivity due to the near-absence of delamination effects. (**b**) Numerical simulation with sub-surface delamination ($\alpha = 0.7$); (**c**) with sub-surface microcracks ($\beta = 0.7$).

17. Two-Dimensional Maps of $|\mathbf{B}|$: Numerical Recovering

Let us preliminarily observe that near the connection points of the tail rudder to the fuselage, the probability of defects occurring is rather high, unlike the central area where this probability is considerably reduced. However, if the onset of defects (even minimal) in the center of the benchmark is detected, the damage will certainly be greater at the connections with the fuselage. Then, in order to have an effective and efficient defect detection device, we assume that each defect is located at the center of the benchmark.

Figure 5b displays the 2D map of the subsurface distribution of $|\mathbf{B}|$ obtained using the proposed numerical approach. It is significant because despite the small amount of α (parameter that weighs the extent of the delamination), the defect is clearly visible and is qualitatively comparable with the similar 2D maps obtained in [9] (and therefore with the 2D maps of the mechanical stress distribution in the CFRP plate). Furthermore, compared to what was obtained in [9], the proposed procedure highlights the defects in a more marked way, considering the procedure as a real alarm system for the presence of even very slight defects. Figure 5c highlights the 2D map of $|\mathbf{B}|$, at the same depth as the previous case, but in the presence of microcracks which are visible even with extremely reduced β. The same observations apply to the porosity (Figure 6a) and to the presence of fiber breaks (Figure 6c) which are clearly visible even if γ and δ are, respectively, extremely reduced. Finally, the concomitance of all the defects simultaneously produces a 2D map of $|\mathbf{B}|$ capable of highlighting the presence of the aforementioned defects. Furthermore, importantly, each type of defect produces a 2D map of $|\mathbf{B}|$ characteristics that can be associated only with that given type of defect. It follows that the proposed approach can act, at least qualitatively, as a sort of defect classifier starting from the distribution of $|\mathbf{B}|$. The ability to distinguish between different types of defects precisely and reliably represents a significant advantage for the maintenance and safety of CFRP materials, especially in critical applications such as aeronautical. The proposed methodology not only improves defect detection, but also offers greater reliability in determining their nature and severity, significantly contributing to the prevention of structural failures.

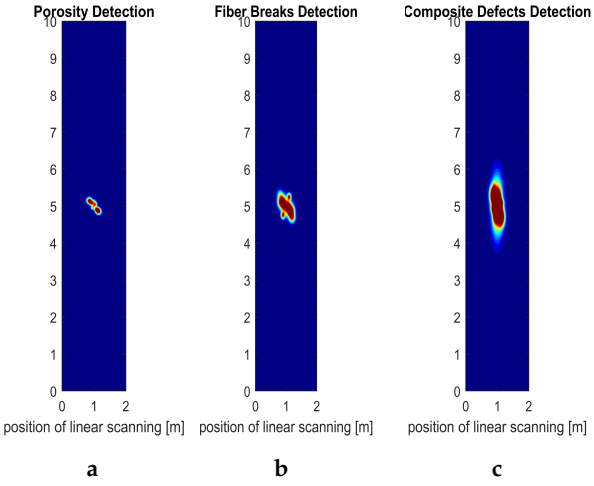


Figure 6. (**a**) With sub-surface porosity ($\gamma = 0.7$); (**b**) numerical simulation with sub-surface fiber cracks ($\delta = 0.7$); (**c**) with all sub-surface defects present, including delamination, microcracks, porosity, and fiber cracks ($\alpha = \beta = \gamma = \delta = 0.7$).

18. Conclusions and Perspectives

In this study, we adapted an Eddy Current (EC) model to characterize subsurface defects in Carbon Fiber Reinforced Polymer (CFRP) plates using approximate solutions via finite element analysis. The defects considered include delaminations, microcracks, porosity, fiber breaks, and the simultaneous presence of these defects. Each defect was modeled as an additive variation in the electrical conductivity tensor of the material, allowing a detailed mathematical representation of the defect's influence on the electromagnetic behavior of CFRP. The proposed model demonstrated a unique and stable solution, with numerical results showing 2D maps of the magnetic induction field that are fully superimposable with those highlighting the distribution of mechanical stress states.

The numerical model was constructed based on the energy functional associated with the complete EC model, ensuring that the numerical approach enjoys the necessary stability. This formulation allowed us to integrate the various energy contributions, ensuring that the

electromagnetic behavior of the material was accurately described and that the obtained solutions were stable and physically consistent. The numerical approach was used to reconstruct the 2D maps of the subsurface distribution of $|\mathbf{B}|$, resulting in defect classification maps and an approximate estimate of their magnitude. These maps are analogous to mechanical stress maps, whose determination is notoriously tricky and requires rather expensive technical instrumentation.

In our analysis, parameters α, β, γ, and δ were considered in isolation in modeling the impacts of structural defects. These parameters weigh the magnitude of each defect: α for delaminations, β for microcracks, γ for porosity, and δ for fiber breaks. However, it is evident that the separate evaluation of each defect may not accurately reflect the cumulative effect when these defects coexist. The simultaneity of defects can amplify the damage beyond the sum of individual effects. Therefore, we intend to develop an integrated model with a multivariate analysis that considers the interactions among the various defects. This model will include interactive coefficients and employ advanced mathematical approaches to more faithfully represent the reality of compromised material.

The proposed methodologies improve defect detection and offer greater reliability in determining their nature and severity, significantly contributing to the prevention of structural failures. The numerical approach used to obtain the 2D maps of $|\mathbf{B}|$ has proven effective in highlighting the presence of even very slight defects, acting as a real alarm system. The ability to distinguish between different types of defects accurately and reliably represents a significant advantage for the maintenance and safety of CFRP materials, especially in critical applications such as aerospace.

Future perspectives include integrating multivariate models and implementing artificial intelligence algorithms to improve defect classification and detection further. These algorithms could learn from the 2D maps of $|\mathbf{B}|$ to identify defects more precisely and predict the evolution of damage over time. Furthermore, additional studies could focus on optimizing the model parameters for different material configurations and operating conditions to make the detection system more robust and versatile.

Therefore, the work carried out represents a significant step forward in non-destructive testing of composite materials. The developed techniques offer high potential for practical applications, improving the safety and reliability of structures made of CFRP materials. The future evolution of the model, with the integration of multivariate analyses and advanced algorithms, promises to make these technologies even more effective and applicable in a wide range of industrial sectors. Finally, a promising future research area might be to introduce scalar and vector degrees of freedom separately into formulation $\mathbf{A} - \phi$. This approach would allow a more detailed analysis of the impact of each component, the vector potential $\mathbf{A}$ and the scalar potential ϕ, on the overall behavior of the system, providing valuable information regarding the differences in terms of numerical stability, convergence, and accuracy of the solution. Everything will be subordinated to the possibility of implementing this separation, starting from the current structure of the mathematical model and its implementation in the numerical code. Otherwise, it is imperative to carry out a significant reformulation of the model. This would allow us to analyze in depth the stiffness matrices and load vectors associated with the vectorial and scalar degrees of freedom and to evaluate how each of them influences the solver's convergence and the solution's precision.

Author Contributions: Conceptualization, M.V., F.L., A.P., F.C.M. and G.A.; methodology, M.V., F.L., A.P., F.C.M. and G.A.; validation, M.V., F.L., A.P., F.C.M. and G.A.; formal analysis, M.V., F.L., A.P., F.C.M. and G.A.; investigation, M.V., F.L., A.P., F.C.M. and G.A.; resources, M.V., F.L., A.P., F.C.M. and G.A.; data curation, M.V., F.L., A.P., F.C.M. and G.A.; writing—original draft preparation, M.V., F.L., A.P., F.C.M. and G.A.; writing—review and editing, M.V., F.L., A.P., F.C.M. and G.A.; visualization, M.V., F.L., A.P., F.C.M. and G.A.; supervision, M.V., F.L., A.P., F.C.M. and G.A.; project administration, M.V., F.L., A.P., F.C.M. and G.A.; funding acquisition, M.V., F.L., A.P., F.C.M. and G.A. All authors have read and agreed to the published version of the manuscript.

Funding: This work has been supported by both the NdT&E Lab, DICEAM Department "Mediterranea" University, Reggio Calabria, Italy; the Italian National Group of Mathematical Physics (GNFM-INdAM) and the University of Messina through FFABR-UNIME 2023.

Data Availability Statement: Data are contained within the article.

Conflicts of Interest: The authors declare no conflicts of interest.

Abbreviations

The following abbreviations are used in this manuscript:

CFRP	Carbon Fiber Reinforced Polymer
EC	Eddy Current
FEM	Finite Element Method
NDT	Non Destructing Testing
PDE	Partial Diffferential Equation

Appendix A. Trace Theorems (for the Proof, See, for Example, [40,45])

Appendix A.1. Trace Theorem form $H(div;\Omega_I)$ onto $H^{-1/2}(\Gamma)$

Mapping $\gamma_n : \mathbf{v} \to \mathbf{v}\cdot\mathbf{n}_{|\Gamma}$ defined on $\overline{\Omega}$ can be extended by continuity to a linear continuous mapping, still denoted by γ_n, from $H(div;\Omega_I)$ onto $H^{-1/2}(\Gamma)$.

Appendix A.2. Trace Theorem from $H^1(\Omega_C)$ onto $H^{-1/2}(\Gamma)$

We let Ω be a bounded open subset of $\mathbb{R}^N$ with boundary $\Gamma \in C^{k,1}$ and let $p \geq 1$ and $s \geq 0$ be two real numbers such that $s \leq k+1$, $s-1/p = l+\sigma$, where $l \geq 0$ is an integer and $0 < \sigma < 1$. Mapping $\mathbf{u} \to \gamma_0\mathbf{u}$ defined on $\overline{\Omega}$ has a unique linear continuous extension as an operator from $W^{s,p}(\Omega)$ onto $Ws-1/p, p(\Gamma)$. Moreover, in $W^{1,p}(\Omega)$, $Ker(\gamma_0) = W_0^{1,p}(\Omega)$.

Appendix B. A Useful Decomposition

Proposition A1. *Let $\boldsymbol{\sigma}'$ be the complex conductivity, ϕ_C the scalar potential, and $\mathbf{v}_C$ the complex vector field. Then, the following identity holds:*

$$\boldsymbol{\sigma}'\nabla\phi_C\cdot\overline{\mathbf{v}}_C + \boldsymbol{\sigma}'\mathbf{v}_C\cdot\nabla\overline{\phi}_C = 2Re(\boldsymbol{\sigma}'\nabla\phi_C\cdot\overline{\mathbf{v}}_C). \tag{A1}$$

Proof. We consider the term $\overline{\sigma}\nabla\phi_C\cdot\overline{\mathbf{v}}_C$. We know that $\mathrm{Re}(\boldsymbol{\sigma}'\nabla\phi_C\cdot\overline{\mathbf{v}}_C)$ represents the real part of the complex dot product. Thus, we can write $\overline{\sigma}\nabla\phi_C\cdot\overline{\mathbf{v}}_C$ as $\boldsymbol{\sigma}'\nabla\phi_C\cdot\overline{\mathbf{v}}_C = \boldsymbol{\sigma}'\nabla\phi_C\cdot\overline{\mathbf{v}}_C$. Now, we consider term $\boldsymbol{\sigma}'\mathbf{v}_C\cdot\nabla\overline{\phi}_C$. We can use the property that the dot product of complex vectors satisfies $\mathbf{a}\cdot\mathbf{b} = \overline{\mathbf{b}\cdot\mathbf{a}}$. Applying this property, we obtain $\boldsymbol{\sigma}'\mathbf{v}_C\cdot\nabla\overline{\phi}_C = \boldsymbol{\sigma}'\overline{\nabla\phi_C\cdot\overline{\mathbf{v}}_C} = \boldsymbol{\sigma}'\overline{\nabla\phi_C}\cdot\overline{\overline{\mathbf{v}}_C}$. Noting that $\overline{\overline{\mathbf{v}}_C} = \mathbf{v}_C$ and $\overline{\overline{\phi}_C} = \phi_C$, we can rewrite $\boldsymbol{\sigma}'\mathbf{v}_C\cdot\nabla\overline{\phi}_C = \boldsymbol{\sigma}'\nabla\phi_C\cdot\overline{\mathbf{v}}_C$. Now, we sum the two terms, $\boldsymbol{\sigma}'\nabla\phi_C\cdot\overline{\mathbf{v}}_C + \boldsymbol{\sigma}'\mathbf{v}_C\cdot\nabla\overline{\phi}_C = \boldsymbol{\sigma}'\nabla\phi_C\cdot\overline{\mathbf{v}}_C + \boldsymbol{\sigma}'\nabla\phi_C\cdot\overline{\mathbf{v}}_C$. Since the two terms on the right-hand side are identical, we can write

$$\boldsymbol{\sigma}'\nabla\phi_C\cdot\overline{\mathbf{v}}_C + \boldsymbol{\sigma}'\mathbf{v}_C\cdot\nabla\overline{\phi}_C = 2\boldsymbol{\sigma}'\nabla\phi_C\cdot\overline{\mathbf{v}}_C. \tag{A2}$$

Now, we observe that $2\overline{\sigma}\nabla\phi_C\cdot\overline{\mathbf{v}}_C$ is equal to $2\mathrm{Re}(\boldsymbol{\sigma}'\nabla\phi_C\cdot\overline{\mathbf{v}}_C)$ since $\boldsymbol{\sigma}'\nabla\phi_C\cdot\overline{\mathbf{v}}_C$ is already a complex number, and multiplying by two yields twice the real part. Therefore, we conclude the following:

$$\boldsymbol{\sigma}'\nabla\phi_C\cdot\overline{\mathbf{v}}_C + \boldsymbol{\sigma}'\mathbf{v}_C\cdot\nabla\overline{\phi}_C = 2\mathrm{Re}(\boldsymbol{\sigma}\nabla\phi_C\cdot\overline{\mathbf{v}}_C). \tag{A3}$$

□

References

1. Silva, M.I.; Malitckii, E.; Santos, T.G.; Vilaça, P. Review of Conventional and Advanced Non-Destructive Testing Techniques for Detection and Characterization of Small-Scale Defects. *Prog. Mater. Sci.* **2022**, *138*, 101155. [CrossRef]

2. Mićić, M.; Brajović, L.; Lazarević, L.; Popović, Z. Inspection of RCF Rail Defects—Review of NDT Methods. *Mech. Syst. Signal Process.* **2023**, *182*, 109568. [CrossRef]
3. Darmon, M. Special Issue on Ultrasonic Modeling for Non-Destructive Testing. *Appl. Sci.* **2024**, *14*, 2008. [CrossRef]
4. Zimermann, R.; Mohseni, E.; Foster, E.A.; Vasilev, M.; Loukas, C.; Vithanage, R.K.; Ding, J. In-Process Non-Destructive Evaluation of Metal Additive Manufactured Components at Build Using Ultrasound and Eddy-Current Approaches. *J. Manuf. Process.* **2023**, *107*, 549–558. [CrossRef]
5. Versaci, M. Fuzzy Approach and Eddy Currents NDT/NDE Devices in Industrial Applications. *Electron. Lett.* **2016**,*52*, 943–945. [CrossRef]
6. Morabito, F.C.; Versaci, M.; Pautasso, G.; Tichmann, C. Fuzzy-Neural Approaches to the Prediction of Disruptions in ASDEX Upgrade. *Nucl. Fusion* **2001**, *41*, 1715–1723. [CrossRef]
7. Cacciola, M.; Morabito, F.C.; Polimeni, D.; Versaci, M. Fuzzy Characterization of Flawed Metallic Plates with Eddy Current Tests. *Prog. Electromagn. Res.* **2007**, *72*, 241–252. [CrossRef]
8. Yang, F.; Dehui, W.; Hao, F. A New Probe-Based Electromagnetic Non-Destructive Testing Method for Carbon Fiber-Reinforced Polymers Utilizing Eddy Current Loss Measurements. *Polym. Compos.* **2023**, *44*, 6661–6675. [CrossRef]
9. Versaci, M.; Angiulli, G.; Crucitti, P.; De Carlo, D.; Laganà, F.; Pellicanò, D.; Palumbo, A. A Fuzzy Similarity-Based Approach to Classify Numerically Simulated and Experimentally Detected Carbon Fiber-Reinforced Polymer Plate Defects. *Sensors* **2022**, *22*, 4232. [CrossRef]
10. Romero-Arismendi, N.O.; Olivares-Galvan, J.C.; Hernez-Avila, J.L.; Escarela-Perez, R.; Jimenez-Mondragon, V.M.; Gonzalez-Montañez, F. Past, Present, and Future of New Applications in Utilization of Eddy Currents. *Technologies* **2024**, *12*, 50. [CrossRef]
11. Tian, G.; Yang, C.; Lu, X.; Wang, Z.; Liang, Z.; Li, X. Inductance-to-Digital Converters (LDC) Based Integrative Multi-Parameter Eddy Current Testing Sensors for NDT&E. *NDT E Int.* **2023**, *138*, 102888.
12. Ryszard, L.; Chady, T. Nondestructive Examination of Carbon Fiber-Reinforced Composites Using the Eddy Current Method. *Materials* **2023**, *16*, 506. [CrossRef] [PubMed]
13. Versaci, M.; Angiulli, G.; Di Barba, P.; Morabito, F.C. Joint Use of Eddy Current Imaging and Fuzzy Similarities to Assess the Integrity of Steel Plates. *Open Phys.* **2020**, *18*, 230–240. [CrossRef]
14. Versaci, M.; La Foresta, F.; Morabito, F.C.; Angiulli, G. A fuzzy divergence approach for solving electrostatic identification problems for NDT applications. *Int. J. Appl. Electromagn. Mech.* **2018**, 57, 133–146. [CrossRef]
15. Angiulli, G.; Versaci, M.; Calcagno, S. Computation of the cutoff wavenumbers of metallic waveguides with symmetries by using a nonlinear eigenproblem formulation: A group theoretical approach. *Mathematics* **2020**, *8*, 489. [CrossRef]
16. Versaci, M.; Angiulli, G.; La Foresta, F.; Laganà, F.; Palumbo, A. Intuitionistic Fuzzy Divergence for Evaluating the Mechanical Stress State of Steel Plates Subject to Bi-axial Loads. *Integr. Comput.-Aided Eng.* **2024**, *31*, 1–17. [CrossRef]
17. Lakhdari, A.E.; Cheriet, A.; El-Ghoul, I.N. Skin Effect Based Technique in Eddy Current Non-Destructive Testing for Thickness Measurement of Conductive Material. *IET Sci. Meas. Technol.* **2019**, *13*, 255–259. [CrossRef]
18. Philibert, M.; Yao, K.; Gresil, M.; Soutis, C. Lamb Waves-Based Technologies for Structural Health Monitoring of Composite Structures for Aircraft Applications. *Eur. J. Mater.* **2022**, *2*, 436–474. [CrossRef]
19. Shetu, M.S.A. Non-Destructive Health Monitoring Techniques for Composite Materials Used in Aerospace Industry. *J. Comput. Mech. Manag.* **2024**, *3* . [CrossRef]
20. Nugraha, A.D.; Nuryanta, M.I.; Sean, L.; Budiman, K.; Kusni, M.; Muflikhun, M.A. Recent Progress on Natural Fibers Mixed with CFRP and GFRP: Properties, Characteristics, and Failure Behavior. *Polymers* **2022**, *14*, 5138. [CrossRef]
21. Rogowski, J.; Kotynia, R. Comparison of Prestressing Methods with CFRP and SMA Materials in Flexurally Strengthened RC Members. *Materials* **2022**, *15*, 1231. [CrossRef] [PubMed]
22. Chen, H.; Na, J.; Wang, D.; Kong, D.; Zhang, X. Numerical Simulation and Failure Experiment of Hygrothermal Aged CFRP Single and Double Lap Joints. *Thin-Walled Struct.* **2023**, *188*, 110786. [CrossRef]
23. Ze, G.K.; Pramanik, A.; Basak, A.K.; Prakash, C.; Shankar, S.; Radhika, N. Challenges Associated with Drilling of Carbon Fiber Reinforced Polymer (CFRP) Composites—A Review. *Compos. Part C Open Access* **2023**, *11*, 100356. [CrossRef]
24. Zhao, Q.; Zhang, K.; Zhu, S.; Xu, H.; Cao, D.; Zhao, L.; Zhang, R.; Yin, W. Review on the Electrical Resistance/Conductivity of Carbon Fiber Reinforced Polymer. *Appl. Sci.* **2019**, *9*, 2390. [CrossRef]
25. Nonn, S.; Schagerl, M.; Zhao, Y.; Gschossmann, S.; Kralovec, C. Application of Electrical Impedance Tomography to an Anisotropic Carbon Fiber-Reinforced Polymer Composite Laminate for Damage Localization. *Compos. Sci. Technol.* **2018**, *160*, 231–236. [CrossRef]
26. Yi, Q.; Wilcox, P. Hughes, R. Modelling and Evaluation of Carbon Fiber Composite Structures using High-Frequency Eddy Current Imaging. *Compos. Part B Eng.* **2023**, *248*, 110343. [CrossRef]
27. Liu, R.Q.; Xum, Z.H.; Yin, J.; Huang, J.J.; Liu, D.; Xie, G.H. A Coupled Mechanical and Electrical Model Concerning Piezoresistive Effect of CFRP Materials. *Compos. Part B Eng.* **2016**, *96*, 125–135. [CrossRef]
28. Forintos, N.; Czigany, T. Multifunctional Application of Carbon Fiber Reinforced Polymer Composites: Electrical Properties of the Reinforcing Carbon Fibers—A Short Review. *Compos. Part B Eng.* **2019**, *162*, 331–343. [CrossRef]
29. Jiao, S.; Li, J.; Du, F.; Sun, L.; Zeng, Z. Characteristics of Eddy Current Distribution in Carbon Fiber Reinforced Polymer. *J. Sens.* **2016**, *12*, 12–26. [CrossRef]

30. Wang, T.; Wu, D. Carbon Fiber Reinforced Polymers, Electrical properties, Eddy current testing, High Frequency. *Compos. Struct.* **2023**, *314*, 116948 [CrossRef]
31. Bui, H.K.; Senghor, F.D.; Wasselynck, G.; Trichet, D.; Fouladgar, J.; Lee, K.; Berthiau, G. Characterization of Electrical Conductivity of Anisotropic CFRP Materials by Means of Induction Thermography Technique. *IEEE Trans. Magn.* **2018**, *54*, 1–4. [CrossRef]
32. Ponomarenko, A.T.; Shevchenko, V.G.; Letyagin, S.V.; Klason, C. Anisotropy of Conductivity in Carbon Fiber-Reinforced Plastics with Continuous Fibers. In Proceedings of the SPIE 2443, Smart Structures and Materials 1995: Smart Structures and Integrated Systems, San Diego, CA, USA, 27 February–3 March 1995.
33. Biro, O.; Valli, A. The Coulomb Gauged Vector Potential Formulation for the Eddy-Current Problem in General Geometry: Well-Posedness and Numerical Approximation. *Comput. Methods Appl. Mech. Eng.* **2007**, *196*, 1890–1904. [CrossRef]
34. Sørensen, B.F. Delamination Fracture in Composite Materials. In *Modeling Damage Fatigue and Failure of Composite Materials*; Woodhead Publishing: Sawston, UK, 2024; pp. 221–251.
35. Zhang, Z.; Hu, L.; Wang, R.; Zhang, S.; Fu, L.; Li, M.; Xiao, Q. Advances in Monte Carlo Method for Simulating the Electrical Percolation Behavior of Conductive Polymer Composites with a Carbon-Based Filling. *Polymers* **2022**, *16*, 545. [CrossRef] [PubMed]
36. Song, X.; Ji, J.; Zhou, N.; Chen, M.; Qu, R.; Li, H.; Wei, Y. Stretchable Conductive Fibers: Design, Properties and Applications. *Prog. Mater. Sci.* **2024**, *144*, 101288. [CrossRef]
37. Muna, I.I.; Mieloszyk, M. Temperature Influence on Additive Manufactured Carbon Fiber Reinforced Polymer Composites. *Materials* **2021**, *14*, 6413. [CrossRef]
38. Gljušćić, M.; Lanc, D.; Franulović, M.; Žerovnik, A. Microstructural Analysis of the Transverse and Shear Behavior of Additively Manufactured CFRP Composite RVEs Based on the Phase-Field Fracture Theory. *J. Compos. Sci.* **2023**, *7*, 38. [CrossRef]
39. Li, W.; Liu, Y.; Jiang, P.; Guo, F.; Cheng, J. Study on Delamination Damage of CFRP Laminates Based on Acoustic Emission and Micro Visualization. *Materials* **2022**, *15*, 1483. [CrossRef]
40. Bossavit, A. *Computational Electromagnetism: Variational Formulation, Complementarity, Edge Elements*; Academic Press: San Diego, CA, USA, 1999.
41. Morisue, T. Magnetic Vector Potential and Electric Scalar Potential in Three-Dimensional Eddy Current Problem. *IEEE Trans. Magn.* **1982**, *18*, 531–535. [CrossRef]
42. Girault, V.; Raviart, P. *Finite Element Methods for Navier-Tokes Equation*; Springer: Berlin/Heidelberg, Germany, 1986.
43. Quarteroni, A.; Sacco, R.; Saleri, F. *Numerical Mathematics*; Springer: Berlin/Heidelberg, Germany, 2010.
44. Van der Vorst, H.A. *Iterative Methods for Large Linear Systems;* Cambridge University Press: Cambridge, UK, 2015.
45. Dautray, R.; Lions, J.L. *Mathematical Analysis and Numerical Methods for Science and Technology. Volume 2: Functional and Variational Methods*; Springer: Berlin/Heidelberg, Germany, 1992.

Disclaimer/Publisher's Note: The statements, opinions and data contained in all publications are solely those of the individual author(s) and contributor(s) and not of MDPI and/or the editor(s). MDPI and/or the editor(s) disclaim responsibility for any injury to people or property resulting from any ideas, methods, instructions or products referred to in the content.